

Energy & Environmental Science

Accepted Manuscript



This is an *Accepted Manuscript*, which has been through the Royal Society of Chemistry peer review process and has been accepted for publication.

Accepted Manuscripts are published online shortly after acceptance, before technical editing, formatting and proof reading. Using this free service, authors can make their results available to the community, in citable form, before we publish the edited article. We will replace this *Accepted Manuscript* with the edited and formatted *Advance Article* as soon as it is available.

You can find more information about *Accepted Manuscripts* in the [Information for Authors](#).

Please note that technical editing may introduce minor changes to the text and/or graphics, which may alter content. The journal's standard [Terms & Conditions](#) and the [Ethical guidelines](#) still apply. In no event shall the Royal Society of Chemistry be held responsible for any errors or omissions in this *Accepted Manuscript* or any consequences arising from the use of any information it contains.

Evaluating different classes of porous materials for carbon capture[†]

Johanna M. Huck,^{ab} Li-Chiang Lin,^a Adam H. Berger,^c Mahdi Niknam Shahrak,^{ad} Richard L. Martin,^e Abhoyjit S. Bhowm,^c Maciej Haranczyk,^e Karsten Reuter,^b and Berend Smit^{*afg}

Received Xth XXXXXXXXXX 20XX, Accepted Xth XXXXXXXXXX 20XX

First published on the web Xth XXXXXXXXXX 200X

DOI: 10.1039/b000000x

Carbon Capture and Sequestration (CCS) is one of the promising ways to significantly reduce the CO₂ emission from power plants. In particular, amongst several separation strategies, adsorption by nano-porous materials is regarded as a potential means to efficiently capture CO₂ at the place of its origin in a post-combustion process. The search for promising materials in such a process not only requires the screening of a multitude of materials but also the development of an adequate evaluation metric. Several evaluation criteria have been introduced in the literature concentrating on a single adsorption or material property at a time. Parasitic energy is a new approach for material evaluation to address the energy load imposed on a power plant while applying CCS. In this work, we evaluate over 60 different materials with respect to their parasitic energy, including experimentally realized and hypothetical materials such as metal-organic frameworks (MOFs), zeolitic imidazolate frameworks (ZIFs), porous polymer networks (PPNs), and zeolites. The results are compared to other proposed evaluation criteria and performance differences are studied regarding the regeneration modes, (*i.e.* Pressure-Swing (PSA) and Temperature-Swing Adsorption (TSA)) as well as the flue gas composition.

1 Introduction

The continuous increase in the world's energy demand has resulted in an increased use of fossil fuels.^{1–3} The burning of these fossil fuels has led to a 30% increase of the carbon dioxide concentration in the last 100 years. To reduce carbon dioxide emissions, Socolow and co-workers⁴ proposed the strategy of wedges in which a wedge represents the implementation of a technology to reduce the carbon emission by 25 billion tonnes over a period of 50 years. To stabilize the emissions at the level of 2006, one needs to implement at least 7 different wedges. In pursuit of this strategy, Carbon Capture and Sequestration (CCS) plays an important role as CCS is one of the few, if not only, viable technologies that can deal with the emissions of fossil fuels. Given that more than 80% of our current energy consumption is based on fossil fuels,⁵ the implementation of new technologies is urgent and CCS is one of the few that can be implemented now. In CCS, carbon

dioxide (CO₂) is captured from the flue gas of a power plant, compressed in order to transport it as a supercritical fluid, and subsequently injected in geological formations.¹ However, the energy intensive separation and subsequent compression as well as the requirement of power plants to build a gas separation unit, are the driving factors in the costs of CCS.

There are two main strategies to capture carbon from the flue gas of a power plant. Depending at which stage the separation process takes place, one refers to the capture process as pre- or post-combustion.^{1,6,7} In pre-combustion, nitrogen (N₂) is removed from the air and nearly pure oxygen is fed into the combustion process in a power plant. As the fossil fuel is burned with nearly pure oxygen, the flue gas contains mainly water and CO₂. Hence, carbon capture can now be performed by simply condensing the water. However, separating oxygen from air is an expensive process, as it requires cryogenic distillation.^{1,6} The post-combustion strategy is to capture the carbon directly from the flue gas of the power plant. The advantage of the post-combustion carbon capture is that it can be added to an existing power plant without the need to retrofit these facilities.^{1,6} Figure 1 gives a process flow sheet of a facility with a post-combustion CCS unit.

At present, three different separation technologies are considered for post-combustion: absorption, membranes, and adsorption.

Natural gas often contains more CO₂ than is allowed in pipelines which requires the CO₂ to be separated. The technology to "sweeten" natural gas has been developed by Bottoms⁸ in 1930 and involves the scrubbing with Mono-Ethanol-

[†] Electronic Supplementary Information (ESI) available: [details]. See DOI: 10.1039/b000000x/

^a Dept. of Chemical and Biomolecular Engineering, University of California, Berkeley, CA 94720; E-mail: berend-smit@berkeley.edu

^b Chair for Theoretical Chemistry and Catalysis Research Center, Technische Universität München, Garching, Germany

^c Electric Power Research Institute, 3420 Hillview Ave, Palo Alto, CA 94304

^d Department of Chemical Engineering, Quchan University of Advanced Technologies, Quchan, Iran

^e Computat. Research Div., Lawrence Berkeley Nat. Lab., Berkeley, CA 94720

^f Materials Sciences Div., Lawrence Berkeley Nat. Lab., Berkeley, CA 94720.

^g Laboratory of molecular simulation, Institut des Sciences et Ingénierie Chimiques, Ecole Polytechnique Fédérale de Lausanne (EPFL), CH-1015 Lausanne, Switzerland.

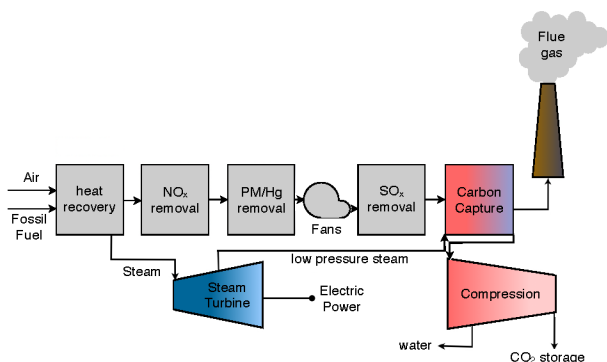


Fig. 1 Schematic diagram of a coal-fired power plant featuring a post-combustion CCS unit. The fossil fuel is mixed with air and burned in a boiler. The generated steam is transformed into electricity through a steam turbine. Nitrogen oxides (NO_x), particulate matter (PM), mercury, and sulfur oxides (SO_x) are removed from the flue gas. Low pressure steam from the steam turbine is used to provide the heating in the carbon capture process. The resulting high purity CO_2 is compressed to final transportation and storage conditions by a compressor. Flue gas residue, mainly N_2 , is emitted into the atmosphere.

Amine (MEA). This technology can be adopted to capture CO_2 from flue gases.^{9,10} Excellent separation performance can be achieved using MEA and other amines but the respective regeneration step is energy intensive. Due to the strong binding of CO_2 to the amines, the amine solutions have to be boiled to remove the CO_2 and regenerate the solvent. At a maximum amine concentration of about 30%, most of the energy is used to boil the water. Although a large fraction of this heat can be recovered, adding the MEA process and subsequent compression to a power plant reduces its efficiency by as much as 30%.^{1,6} In addition, the oxygen in the flue gas causes the amines to degenerate. At present, however, amine scrubbing is the only technology that is sufficiently advanced to be applied in CCS today. Finding alternative technologies aimed at mitigating some of the disadvantages of these amine solutions is an active area of research which focuses on membrane and adsorption technologies.

Membrane separations are based on differences in the permeability of different components.^{1,6} The driving force for membrane separation comes from the difference in the components' partial pressures on the two sides of the membrane. As post-combustion carbon capture is an end-of-pipe technology, the pressure of the flue gas is too low for a sufficient pressure gradient. This can be remedied by compressing the flue gases or pulling vacuum which, however, requires a significant amount of energy due to the large flue gas volumes involved in the separation.¹¹ The flue gas can be compressed or pressurized five-fold by using 10-20% of the produced energy for compression or pulling vacuum.¹² These practical limitations

have important consequences for the design of a membrane separation process.¹² Hence, finding novel membrane materials is of great interest to the whole scientific community.¹³⁻¹⁹

Alternatively, CO_2 can be captured through adsorption in the pores of solid materials.²⁰⁻²² This technology takes advantage of the preferential adsorption of CO_2 in the pores of adsorbents compared to other flue gas components. Nanoporous materials – like zeolites,²³ zeolitic imidazolate frameworks (ZIFs),²⁴ porous polymer networks (PPNs),²⁵ and metal-organic frameworks (MOFs)²² – can have large internal surfaces and high selectivities towards CO_2 depending on their structure and composition.²⁰ Particularly, MOFs have attracted great attention due to the enormous number of possible combinations of the different metals and organic linkers.^{20,22} To date, over 5,000 different MOFs have been synthesized.²⁶ The sparked interest is evident in the number of published articles with MOFs as main topic which has increased by a factor seven between 1999 and 2007.

Such a large number of materials raises the important practical question which criteria are best suited to evaluate their performance. For most people the answer to this question will be related to the cost increase of electricity caused by implementing CCS. The best material will be the one for which the full life cycle analysis gives the smallest increase in the price of electricity. Many of the materials that we are investigating in this work, however, are in such an early stage of research that we simply do not have any insights in the overall costs of the complete process. It is therefore important to develop a next best criterion that captures some of the key aspects that contribute to the cost of a carbon capture process that uses this material.

Comparing the liquid absorption with a solid adsorption process, the important difference to note is the relative simplicity with which a liquid can be transported. As a consequence it is also simple to develop a continuous process which includes full heat integration. This allows us to recover the heat required to regenerate the absorbent. In a solid process, however, heat integration is more difficult to realize which is why one has to ensure the minimization of the energy required to regenerate the adsorbent. Another important CCS contribution which needs to be included in the evaluation of a material is the cost caused by the compression of CO_2 for geological storage. Given that energy requirements contribute significantly to the overall cost of carbon capture, one would never consider a novel adsorbent with energy requirements significantly higher than the current MEA process. A first screening would hence be based on the prediction of the total energy penalty imposed on a power plant by applying CCS. This concept of an energy penalty or parasitic energy was first introduced by Rochelle and co-workers in 2009.²⁷ The characteristic of parasitic energy is to express the energy requirement for flue gas separation and subsequent CO_2 compression in

terms of loss in electricity production.

This work concentrates on the performance of porous materials for a post-combustion CCS process in power plants using a Temperature-Pressure-Swing Adsorption (TPSA) process. We compare different materials and criteria that have been proposed to evaluate the potential performance of these materials. In this comparison we look at capturing CO₂ from the flue gas of coal and natural gas fired power plants, and carbon capture directly from air.

2 Carbon Capture Process

2.1 Adsorption Process

Figure 2 illustrates the four subsequent steps in an adsorption process. We start with a clean, regenerated bed. During the adsorption step flue gas flows through the bed and the CO₂ selectively adsorbs, leaving a N₂ rich exhaust stream. Once the bed is saturated the bed needs to be regenerated. This can be done by applying a vacuum and/or by increasing the temperature to conditions where the CO₂ desorbs resulting in a CO₂ rich stream for subsequent sequestration. The process is called Pressure Swing Adsorption (PSA) and Temperature Swing Adsorption (TSA) if we use pressure and temperature, respectively. It is also possible to increase both the temperature and change the pressure called a Temperature-Pressure-Swing Adsorption (TPSA) process. In addition, it should be noted that compression of the CO₂ rich stream is required for transportation and sequestration.

Several methods to evaluate materials for their CCS performance have been proposed.^{28–30} These methods typically use adsorption related properties such as the uptake, selectivity, working capacity, breakthrough time, surface area, or porosity as criteria to rank materials.^{30–36} Most of these criteria aim to maximize the adsorption capacity of a material, or aim to correlate the performance to structural properties like surface area, pore volume, and pore size. As we will show in this work, the difficulty with these single property criteria lies in the assumption that the materials all perform optimally at the conditions for which we compare the performance. Moreover, a CCS process requires CO₂ sequestration at high pressures, whereas, for instance, optimization of adsorption capacity or breakthrough time only focuses on the adsorption process but does not consider the regeneration and compression steps. To address these issues, we used parasitic energy as a metric which also takes into account to optimization of desorption conditions in the design of a separation process. The metric is a measure for the loss of electricity caused by the addition of a CCS process to an existing power plant with respect to a given solid adsorbent. In this context, the best material is the one that minimizes the parasitic energy. This results in a more abstract metric difficult to relate to material properties which

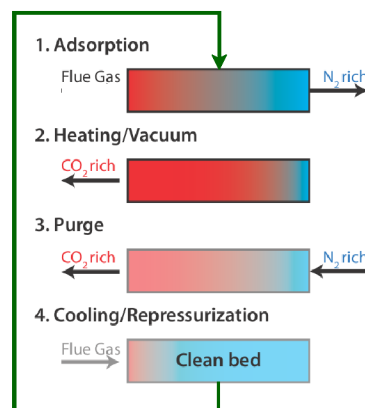


Fig. 2 Four steps in a temperature and pressure swing adsorption process. In the first step CO₂ adsorption takes place while flue gas pervades the solid adsorbent. N₂ enriched gas leaves the bed. To initiate the regeneration process the solid bed is heated up and evacuated in the second step. CO₂ is forced to desorb from the surface and CO₂ rich gas is exiting the adsorbent. In step three the solid is purged by N₂ gas to get rid of the left over CO₂ residue. The final step serves as preparation for the next adsorption cycle. The adsorbent is cooled down and pressurized until adsorption conditions are reached again.

is why it is instructive to compare parasitic energy to the more conventional criteria.

2.2 Energetics of Carbon Capture

In the following we discuss the parasitic energy metric in detail and compute the minimal energy required to carry out a two-component gas separation.

2.2.1 Parasitic Energy. In our simplified process the total energy required to perform CCS is composed of two parts: the heat required to carry out the separations and the energy spent to compress the captured CO₂ up to 150 bar. The former consists of two terms: (1) the energy needed to heat up the adsorbent to reach the desorption conditions (sensible heat), and (2) the energy required to undo the adsorption process. For the endothermic process of CO₂ desorption we need to supply energy that is equivalent to the heat of adsorption (Δh). The total thermal energy Q_{thermal} per kilogram captured CO₂, m_{CO_2} is hence given by:

$$Q_{\text{thermal}} = \frac{C_p \cdot m_{\text{adsorbent}} \cdot \Delta T}{m_{\text{CO}_2}} + \frac{\Delta h_{\text{CO}_2} \cdot \Delta \sigma_{\text{CO}_2} + \Delta h_{\text{N}_2} \cdot \Delta \sigma_{\text{N}_2}}{m_{\text{CO}_2}} \quad (1)$$

The first term corresponds to the sensible heat requirement which drives the process through heating up the bed. It can be calculated using the specific heat capacity C_p of the adsorbent, the total mass of the adsorbent $m_{\text{adsorbent}}$, and the tempera-

ture difference between adsorption and desorption conditions ($T_{\text{final}} - T_{\text{flue}}$). The second part of the thermal energy represents the energy needed to desorb both gases, CO₂ and N₂, which consists of the working capacities $\Delta\sigma_i$ multiplied by the heat of adsorption Δh_i for each flue gas component. The working capacity is defined as the difference in amount adsorbed at flue gas conditions (1 atm, 40°C) and left in the material at desorption conditions. Note that we calculate m_{sorbent} in equation 1 as $\rho \cdot (1 - \varepsilon) \cdot V$ using the sorbent's density ρ , a fixed void fraction ε of 0.35, and a fixed volume V of 1 m³.

The second contribution to the parasitic energy involves the compression of CO₂ to transport and storage conditions (150 bar).¹ A model of a multi-stage compressor was used to estimate the pumping work to compress our captured gas. A maximum pressure ratio of each stage was set to 2.5 to avoid an extreme temperature increase of the captured gas. Additionally, the gas was cooled to 40°C between each compression cycle. The isentropic efficiency of the pump was assumed to be 85% for gas below the supercritical point and 90% above it. The model is based on data which captures the real fluid properties of mixtures with different purities and their changing behavior at the critical point during compression. We obtained the data using NIST REFPROP.³⁷ This database includes the equation of state³⁸ for fluid mixtures containing different gas components, like CO₂, N₂ and others. Additionally, the compression energy mainly depends on the CO₂ gas purity and the gas pressure at which desorption takes place. Thus, to make the model practical for screening, we developed a functional representation to estimate the compression work for a range of desorption pressures and CO₂ purities. This allowed us to avoid using REFPROP for every single combination of CO₂ purity and desorption pressure.³⁹ Note that, in general, two separate pumping contributions are involved in our process. On the one hand, there is the pumping work to evacuate the sorbent to realize the desorption pressure below 1 atm. In addition, we also need pumping work to compress the captured gas from desorption pressure to 150 bar. In reality, however, both happen in parallel. While compressing captured gas from desorption pressure (below 1 atm) to storage conditions, the pump also creates a low-pressure which we use in the pressure swing operation to reach desorption pressure. Hence, we do not have to count both contributions but only the main pumping cost created by compressing the gas from desorption conditions to 150 bar.

Moreover, in our model we assume that steam from the power plant is used as heat source and that the compressors are driven by the produced electricity directly. As steam is not converted with 100% efficiency into electricity, we need to multiply the heat requirement with the Carnot efficiency $\eta_{\text{carnot}} = 1 - T_c/T_h$ and the efficiency of a gas turbine (75%):⁴⁰

$$E_{\text{parasitic}} = (0.75 Q_{\text{thermal}} \cdot \eta_{\text{carnot}}) + W_{\text{comp}} \quad (2)$$

In this equation, the implicit variable is the desorption condition. The desorption condition not only determines the working capacity but also the CO₂ purity for the compression energy. For example, by changing the desorption temperature one can ensure identical working capacities of two materials. Still, the material with the lower desorption temperature will have a lower parasitic energy due to the cooler steam required. As an alternative one can obtain the same working capacities by changing the desorption pressure; the one with the lowest compression cost would then be the best material. Hence, the optimal desorption conditions are those that minimize this parasitic energy.

2.2.2 Minimum Energy. We can use elementary thermodynamics to calculate the minimum energy of separating CO₂ from a two-component gas mixture. It is reasonable to approximate flue gas as an ideal gas mixture. We can therefore estimate the minimum energy requirement from the ideal gas entropy of mixing.¹¹

The molar entropy of an ideal gas mixture containing a mole fraction x of CO₂ is given by:

$$s^{\text{im}}(x) = -R[x \ln x + (1 - x) \ln(1 - x)] \quad (3)$$

where R is the gas constant.¹ If we assume that the separation is carried out at a temperature of T_{sep} , the minimal energy required for the separation can be determined using the captured, emitted, and the flue gas entropies via:

$$-W_{\text{min}}^{\text{sep}} = T_{\text{sep}} \Delta S \quad \text{with} \\ \Delta S = n_{\text{em}} s^{\text{im}}(x_{\text{em}}) + n_{\text{cap}} s^{\text{im}}(x_{\text{cap}}) - n_{\text{flue}} s^{\text{im}}(x_{\text{flue}}) \quad (4)$$

where n_{cap} and n_{em} are the number of moles of the captured and emitted gases, respectively. Total and compositional mass balances are as follows.

$$n_{\text{flue}} = n_{\text{cap}} + n_{\text{em}} \quad (5) \\ x_{\text{flue}} n_{\text{flue}} = x_{\text{cap}} n_{\text{cap}} + x_{\text{em}} n_{\text{em}} \quad (6)$$

In this work, we assume that adsorption takes place at constant coal flue gas conditions, namely 40 °C, 1 atm, and 14 : 86 (CO₂:N₂), resulting in $W_{\text{min}}^{\text{sep}} = 171.1$ kJ/kgCO₂ to separate pure CO₂ out from flue gas. This value is comparable to $W_{\text{min}}^{\text{sep}} = 175.8$ kJ/kgCO₂ reported by Bhowan et al.¹¹ at an initial flue gas composition of 13 : 87. In the process of carbon capture, we assume that the captured gas exhibits a purity of 99% which yields in a minimum work requirement of $W_{\text{min}}^{\text{sep}} = 167.7$ kJ/kgCO₂. Details on the calculation and the assumptions can be found in the supporting information.

Next, we need to add the energy required to compress the captured gas to the typical pressure in transport and geological storage. Using a compressor model as described in section 2.2.1, results in a minimum compression work of

$$W_{\min}^{\text{comp}} = 357.7 \text{ kJ/kgCO}_2.$$

Before we can combine minimal separation and compression work to allow for a reasonable comparison to parasitic energies, we need to convert the minimum separation work to the power plant's electricity output. Assuming heat as source for the separation energy a maximum thermal efficiency of 40%⁴¹ can be applied to obtain a total minimal energy requirement of 424.8 kJ/kgCO₂. We make this assumption for convenience but using a low pressure steam turbine would result in a lower theoretical minimum, of course.

2.3 Thermodynamics of adsorption

For the computation of parasitic energy we need to determine several thermodynamic properties of the system. The most important ones are the (mixture) adsorption isotherms from which we can obtain the working capacities and the purity of captured CO₂ as a function of desorption conditions.

Pure component isotherms for N₂ and CO₂ were obtained by fitting dual- or single-site Langmuir isotherms to experimental adsorption data if available, or to data from molecular simulation. Langmuir isotherms with N sites are given by

$$\sigma_i = \sum_{j=1}^N \frac{k_{H,i,j} \cdot p_i}{1 + \frac{k_{H,i,j}}{\sigma_{\text{sat},i,j}} \cdot p_i} \quad (7)$$

with σ_i the loading at partial pressure p_i , $k_{H,i,j}$ the Henry coefficient, and $\sigma_{\text{sat},i,j}$ the saturation loading of component i and corresponding adsorption site j . We assume that saturation loadings and heat of adsorption h are temperature independent. Hence, the temperature dependence of the Henry coefficients follows directly from the van't Hoff relation:

$$\ln k_{H,i,j}(T) = A - \frac{\Delta h_{i,j}}{RT} \quad (8)$$

We used two different models to predict the mixture adsorption based on the known pure component isotherms. The Ideal Adsorbed Solution Theory (IAST)⁴² and the Competitive Langmuir Adsorption model were implemented into the parasitic energy metric to identify potential performance differences. The former is employed for almost all parasitic energies presented in this paper. A detailed comparison between these two models can be found in the supporting information. IAST is a commonly used method to predict the behavior of gas mixtures in the adsorbed phase and corresponding loadings can be determined by subsequently applying equation 7. On the contrary mixture isotherms for single site materials on basis of the Competitive Langmuir model can be estimated by using

$$\sigma_1 = \frac{k_{H,1} \cdot p_1}{1 + \frac{k_{H,1}}{\sigma_{\text{sat},1}} \cdot p_1 + \frac{k_{H,2}}{\sigma_{\text{sat},2}} \cdot p_2} \quad (9)$$

where indices 1 and 2 represent the flue gas components CO₂ and N₂, respectively. For dual-site adsorption, the stronger site was assumed to exclusively adsorb CO₂, while N₂ is only competing for the weaker CO₂ site. The following equations show the dual-site and single-site approach for CO₂ and N₂ where indices 1 and 2 indicate the stronger and weaker site, respectively.

$$\sigma_{\text{CO}_2} = \frac{k_{H,\text{CO}_2,1} \cdot p_{\text{CO}_2}}{1 + \frac{k_{H,\text{CO}_2,1}}{\sigma_{\text{sat},\text{CO}_2,1}} \cdot p_{\text{CO}_2}} + \frac{k_{H,\text{CO}_2,2} \cdot p_{\text{CO}_2}}{1 + \frac{k_{H,\text{CO}_2,2}}{\sigma_{\text{sat},\text{CO}_2,2}} \cdot p_{\text{CO}_2} + \frac{k_{H,\text{N}_2,1}}{\sigma_{\text{sat},\text{N}_2,1}} \cdot p_{\text{N}_2}} \quad (10)$$

$$\sigma_{\text{N}_2} = \frac{k_{H,\text{N}_2,1} \cdot p_{\text{N}_2}}{1 + \frac{k_{H,\text{N}_2,1}}{\sigma_{\text{sat},\text{N}_2,1}} \cdot p_{\text{N}_2} + \frac{k_{H,\text{CO}_2,2}}{\sigma_{\text{sat},\text{CO}_2,2}} \cdot p_{\text{CO}_2}} \quad (11)$$

Furthermore, in the Competitive Adsorption model the single-site approach assumes equal saturation loadings for both flue gas components. The same applies for the dual-site adsorption, the only difference being that the loading of the weaker CO₂ site equates the N₂ loading. These assumptions are made for thermodynamic consistency.⁴³ With the pure component isotherms at our disposal, IAST or Competitive Adsorption model allow us to compute the equilibrium composition in the adsorbent as a function of temperature and pressure, from which we can obtain the working capacities of CO₂ and N₂ as well as the purities of capture and emission gases.

Table 1 lists the specific heat capacities C_p for a selection of MOFs and zeolites. These are needed in equation 2 but only known for a handful of materials. As can be seen from table 1, it is important to note that the values for C_p are similar and generally range from $C_p = 0.761 - 1.21$ J/gK. For all materials in this work, we therefore used a mean $C_p = 0.985$ J/gK and discussed resulting uncertainties in the supporting information. It is also assumed that adsorbed gases and temperature do not influence the heat capacities.

Table 1 Heat capacities C_p of various MOFs & zeolites at 333 K.

material	C_p / J/gK	material	C_p / J/gK
BEA	0.830 ^{44,45}	MOF-5	0.761 ⁴⁶
MFI	0.863 ^{44,45}	MOF-177	0.840 ⁴⁶
MTT	0.841 ^{44,45}	UMCM-1	0.851 ⁴⁶
LaCu-MOF	1.21 ^{46,47}		

For the optimization process in TPSA, we fixed the ranges of desorption pressure and temperatures to 0.01 atm < p_{des} < 3 atm and 333 K < T_{des} < 473 K, respectively. As TSA operates at constant pressure conditions, the desorption conditions were set to $p_{\text{des}} = 1$ atm (equals adsorption pressure) and 333 K < T_{des} < 473 K. In contrast, PSA is characterized by a constant temperature and desorption conditions were kept at $T_{\text{des}} = 333$ K and 0.01 atm < p_{des} < 3 atm.

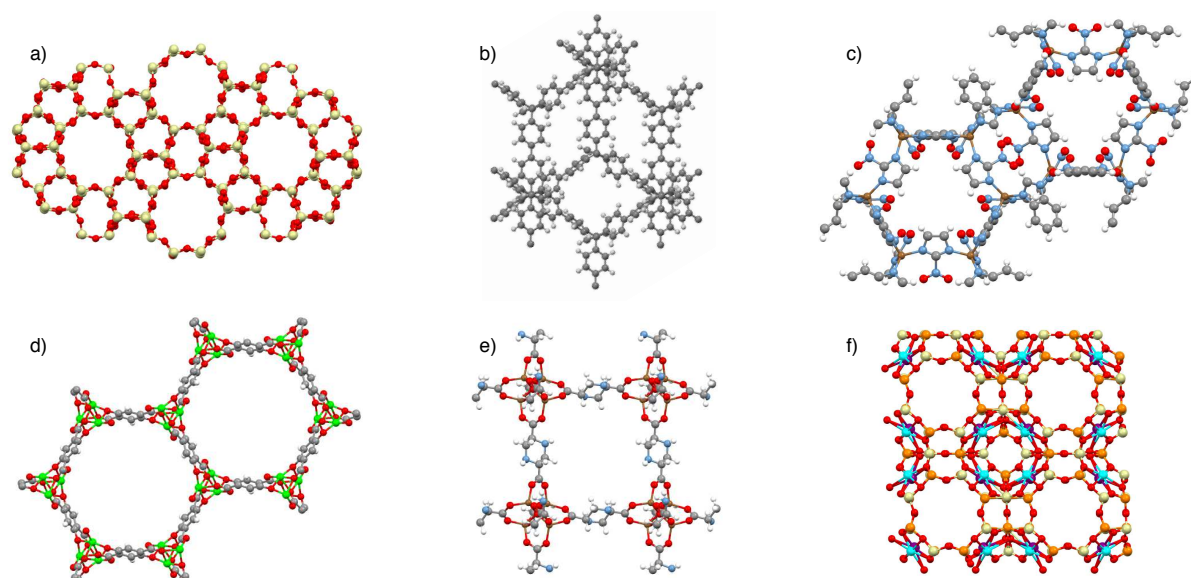


Fig. 3 Representative selection of structures for each material class under investigation: a) MFI, b) PPN-6, c) ZIF-78, d) Mg-MOF-74, e) HMOF-992, and f) CaA. Atoms and bonds are illustrated as ball and sticks. Color-code for the atoms: red: oxygen, yellow: silicon, grey: carbon, white: hydrogen, blue: nitrogen, green: magnesium, brown: zinc, orange: aluminium, cyan: calcium, and purple: sodium.

3 Material selection

We have selected five different classes of porous materials for performance analysis via parasitic energy that have been reported in the recent literature for their potential for carbon capture: zeolites,²³ zeolitic imidazolate frameworks (ZIFs),^{36,48,49} cation exchanged zeolites (CEZs),⁵⁰ porous polymer networks (PPNs),^{51,52} and metal-organic frameworks (MOFs).^{20–22,34,51–64} MOFs and PPNs, in particular, exhibit improved adsorption properties^{65,66} and hence, might indicate promising performance in parasitic energy. MOFs stand out due to their nearly infinite number of possible structures by varying metals and framework components. We also include MOFs with open metal site; the series of M-MOF-74, CuBTC, and CuBTri,^{31,35,67–69} which exhibit even higher CO₂ uptake capacities. These open metal sites arise from removing coordinated solvent molecules and are known to create preferential adsorption sites for CO₂.^{58,70} In addition, recent literature^{62–64} has highlighted two pyrazine based and hexafluorosilicate anion bridged isostructural MOFs from the SIFSIX-3-M series as very promising candidates for CO₂ removal, particularly for direct air capture. The class of PPNs, on the other hand, attracts attention by its widely open and accessible pores.⁵² Tetrahedral phenyl-based monomers form a diamondoid network which is suitable to introduce CO₂-cohesive extra-framework molecules to increase the CO₂ affinity.^{51,66} In this work, we particularly concentrate on PPN-6 based structures tethered with different polyamines. We also investigated the CCS performance of CEZs to determine the impact

of varying the framework type and partially exchanging the containing cation. The two analyzed frameworks count to the Linde type A (NaA) and the Linde type X (NaX). The Na cation in the two framework types were partially exchanged by Mg- and Ca-cations. Additionally, we included a class denoted as hypothetical, containing materials which were theoretically predicted but are not known to be synthesized, yet. Several hypothetical MOF materials based on the familiar material MOF-5⁷¹ and hypothetical ZIF structures are part of this class. Figure 3 shows a representative structure for each class of materials we studied in this work.

4 Carbon capture of flue gas from coal

In subsection 4.1, we calculate and discuss the parasitic energy for TPSA for carbon capture from a coal fired power plant. Subsection 4.2 studies the consequences of separate temperature and pressure swings on parasitic energy and working capacity. We conclude in subsection 4.3 by comparing our results to a selection of other metrics suggested in literature.

4.1 Parasitic energy in TPSA

Figure 4 shows the parasitic energy from a coal fired power plant using an adsorption process for the materials in section 3 as a function of their CO₂ Henry coefficient (k_{H,CO_2}).

It is interesting to compare these results with the corresponding parasitic energy of the currently applied MEA

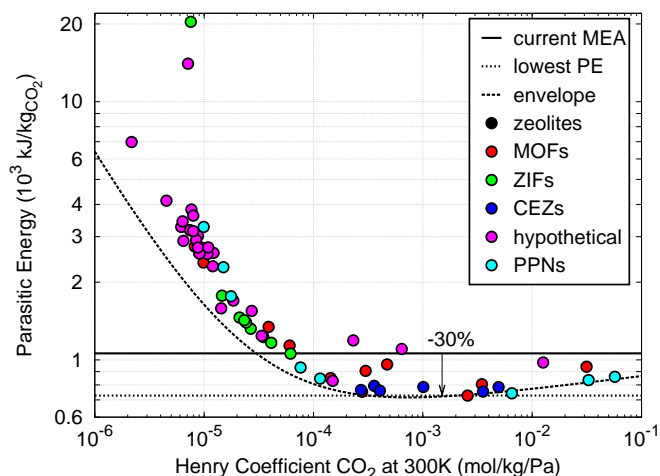


Fig. 4 Parasitic energy to capture CO₂ from coal flue gas as function of the CO₂ Henry coefficient (k_{H,CO_2}) at 300 K. Circles depict parasitic energy results for each material. Current MEA technology is marked as solid line. The dashed line shows an envelope for coal based on a large library of hypothetical zeolites. The dotted line indicates the lowest predicted parasitic energy, namely Mg-MOF-74 at 727.12 kJ/kgCO₂.

technology for coal flue gas which is estimated to be at 1,060 kJ/kgCO₂ based on similar assumptions as our model.⁷² This value is about 300 kJ/kgCO₂ lower than the originally reported one which additionally considers energy losses caused by equipment.⁴¹ In our parasitic energy calculation we also ignore these contributions. We see that there are quite a number of materials that have a parasitic energy below the current technology which is an important and encouraging result. Amongst them are most of the CEZs, open metal site and both SIFSIX-3-M MOFs as well as the PPN-6 based structures. In the selection of materials in table 2, Mg-MOF-74 stands out as the one with the lowest parasitic energy (727 kJ/kgCO₂). The amine functionalized MOF mmen-CuBTTri has a comparable parasitic energy of 752 kJ/kgCO₂. Compared to MEA, an adsorption process with these materials could reduce the parasitic energy of a CCS process by up to 30%.

The theoretical minimum energy required to separate CO₂ from a gas mixture equals 425 kJ/kgCO₂ as calculated in section 2.2 and is about 300 kJ/kgCO₂ lower than our best performing material Mg-MOF-74. However, the sensible heat and the desorption heat have to be considered in a real adsorption case in addition to the actual separation. Comparing the MOF's effective heating requirement (142 kJ/kgCO₂) and the minimal separation energy (67 kJ/kgCO₂, after applying the thermal efficiency) shows that sensible and desorption heat account for approximately 80 kJ/kgCO₂. Hence, the main energy difference (≈ 220 kJ/kgCO₂) results from the compression work which for both, the theoretical minimum and Mg-MOF-

Table 2 Selection of materials with the lowest parasitic energies (in kJ/kgCO₂) for coal flue gas (CO₂ : N₂ = 14 : 86) sorted by decreasing performance. All other parasitic energy results can be found in the supporting information.

material	PE	material	PE
Mg-MOF-74	727	CaX	785
PPN-6-CH ₂ TETA	742	MgA	793
mmen-CuBTTri	752	SIFSIX-3-Zn	805
NaX	754	ZIF-36-FRL	829
MgX	760	PPN-6-CH ₂ TAEA	835
NaA	765	PPN-6-SO ₃ Li	846
CaA	784	Zn-MOF-74	850

74, is based on the same model calculations with desorption pressures of 1 atm and 0.1 atm, respectively. A desorption pressure difference of only one order of magnitude thus affects the compression work significantly.

We also compared the parasitic energies of our material selection to an extensive screening of a library of zeolites which consists of experimentally known and theoretically predicted (hypothetical) zeolites.⁷² The dashed line in figure 4 indicates the lowest parasitic energy of all zeolite materials with a given CO₂ Henry coefficient. It highlights the existence of an optimal range of Henry coefficients ($\sim 10^{-4} - 10^{-2}$ mol/kgPa). Lower Henry coefficients result in lower working capacities, and higher coefficients require too much energy in the regeneration step.⁷² The experimental structures follow the same trends. Most of the ZIFs and hypothetical MOFs populate the low Henry coefficient region, and hence have a relatively high parasitic energy. Materials with a very high Henry coefficient (mainly amine appended PPNs and SIFSIX-3-Cu) still exhibit comparably low parasitic energies, but already are precursor to a steadily increasing trend. The region of optimal Henry coefficients includes CEZs and open metal site MOFs. Materials with parasitic energies of more than 2,000 kJ/kgCO₂ mainly include the hypothetical structures, but also some of the MOFs (*i.e.*, UMCM-1, MOF-177), PPNs (*i.e.*, PPN-4 and PPN-6), and ZIF-8. Even though all of these structures exhibit high surface areas and porosities they are expected to perform less in CCS due to their low Henry coefficients. Particularly, ZIF-8 prefers the adsorption of N₂ over CO₂ which is why an extremely high parasitic energy of 20,000 kJ/kgCO₂ is predicted for it.

It is interesting to investigate the effect of changes in parasitic energy in the MOF-74 series by varying the metal center. Looking at Mg, Zn, Co, and Ni as metal centers the according MOFs turn out to rank in the order Mg-MOF-74 < Zn-MOF-74 < Co-MOF-74 < Ni-MOF-74. The exceptional performance of Mg-MOF-74 by up to hundreds of kilojoules traces back to its higher density of open metal sites.³⁵

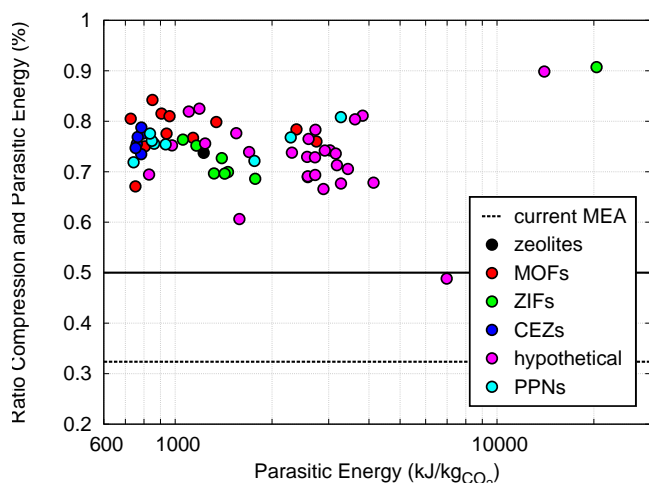


Fig. 5 Contribution of heating energy and compression work to total parasitic energy in case of coal flue gas. The solid line marks an even contribution of both energy requirements and the dashed line denotes the state-of-art technology amine-scrubbing.

For the PPN-6 family we observed that all functionalized PPN-6 materials perform significantly better in parasitic energy than bare PPN-6. In the case of sulfonic functional groups, the sulfonic acid grafted PPN-6 is outperformed by its lithium salt. Even lower parasitic energies can be obtained by controlling the amine functionalizing of PPN-6 with respect to number of amine groups and chain length: PPN-6-CH₂TETA < PPN-6-CH₂TAEA < PPN-6-CH₂DETA.

Comparison of different CEZ structures shows that changing the cation has a large effect on the Henry coefficient, but causes little change in the parasitic energy. In general, the Linde type X materials perform slightly better than the Linde type A structures with NaX leading the ranking. All zeolites in this range and their respective rank are listed in table 2.

It is instructive to see how the separation and the compression contribute to the parasitic energy. Figure 5 shows the fraction the compression energy contributes to the total parasitic energy. For the MEA process the compression costs contribute 32%. This comparably low contribution results mainly from the predominating heating requirement to produce pure CO₂ for storage by removing the water content. The required compression work is also lower due to an initial CO₂ pressure of 1-2 atm. In comparison, the compression contribution of our best materials ranges between 65-85% as CO₂ gas from below 1 atm needs to be compressed up to 150 bar. For the materials like ZIF-8 and the hypothetical HMOF-96 with high parasitic energies (> 10,000 kJ/kgCO₂), the share of compression work can be as much as 90%. These materials adsorb preferentially N₂ which results in higher compression requirements due to low CO₂ purities.

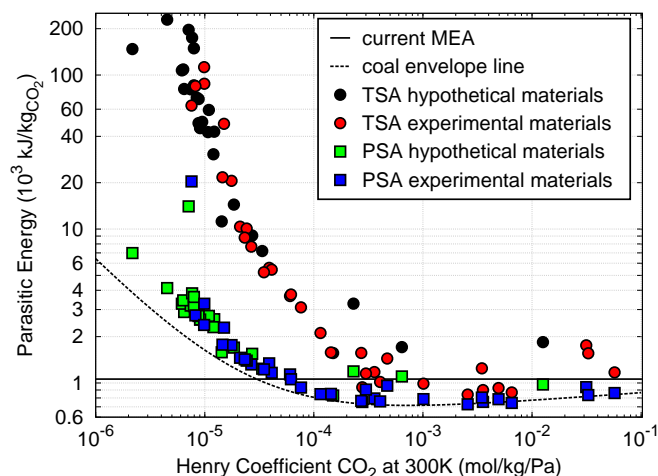


Fig. 6 Comparison between parasitic energies computed in pure PSA and TSA regeneration mode.

4.2 Parasitic energy in PSA vs. TSA

In the previous section we optimized the parasitic energy using a hybrid pressure swing/temperature swing process, *i.e.* the working capacity of a material can be optimized by both changing the temperature and pressure at which regeneration takes place. One does not always have the possibility to carry out such a hybrid scheme and it is therefore interesting to look at the parasitic energy if only TSA or PSA is applied. Figure 6 shows the parasitic energy results for capturing CO₂ from coal flue gas in dependence of the Henry coefficient at 300 K using TSA and PSA as regeneration strategies. The respective operating conditions are outlined in subsection 2.3.

Figure 6 suggests that regenerating nano-porous materials using the PSA strategy always leads to lower energy loads compared to TSA. In the latter, the emphasis is put on optimizing the heating energy which is directly linked to the working capacity. Compression costs, however, are almost steady due to the fixed desorption pressure conditions. Unlike TSA, PSA is designed to optimize the compression requirements for a given working capacity due to the fixed desorption temperature conditions. For materials with a low Henry coefficient (10⁻⁶ – 10⁻⁴ mol/kgPa) the working capacity is small. This requires one to heat up the entire sorbent to relatively high temperatures to even enable the capture of a small amount of CO₂ resulting in very high heating costs in TSA. In a PSA, a small working capacity does not have a dramatic effect on the parasitic energy as the compression cost is the predominating and a very sensitive energy requirement (see subsection 4.1). However, applying PSA does increase the capital costs due to higher sorbent demand. Table 3 highlights these observations along with the total parasitic energies for materials with low and high Henry coefficients. The parasitic energies of both re-

Table 3 Difference between heating and compression requirement for PSA & TSA regeneration mode. Material selection covers the whole Henry coefficient spectrum. For all materials, see supporting information.

material	PSA / MJ/kgCO ₂		
	heating	compression	total
Mg-MOF-74	0.14	0.59	0.73
PPN-6-CH ₂ DETA	0.21	0.65	0.86
ZIF-69	0.38	1.0	1.4
ZIF-8	1.9	18	20

material	TSA / MJ/kgCO ₂		
	heating	compression	total
Mg-MOF-74	0.46	0.38	0.84
PPN-6-CH ₂ DETA	0.81	0.36	1.2
ZIF-69	9.4	0.72	10
ZIF-8	47	16	63

generation strategies become comparable for materials with a large Henry coefficient while generally tending to lower parasitic energies in PSA. The dotted line in figure 6 compares TSA and PSA with the optimal TPSA results. The close agreement with the PSA results shows that the whole process tends to favor the use of PSA.

In our metric, the working capacity plays an important role in the TSA's but less in the PSA's parasitic energies. However, a low working capacity influences the capital costs which mandates a separate look at the working capacity. Figure 7 shows a high working capacity for the optimal materials in both strategies. Interestingly, in the high Henry coefficient region, TSA exhibits higher worker capacities but higher parasitic energies. This figure also illustrates the limitation of our metric: we may identify a material that is interesting from an operation cost but not from a capital cost point of view. Moreover, our metric does not consider any transport restrictions. For instance, we assume that adsorption and desorption of CO₂ happen instantaneously. However, two materials with identical thermodynamic properties will result in identical parasitic energies. If it takes twice as long to complete a full capturing cycle, the capital costs of the material that takes longer might be twice as high due to the required increase in adsorbers to keep up with the flue gas flux of the power plant.

4.3 Comparison of parasitic energy to other metrics

Bae et al. investigated 25 different materials to evaluate their suitability for capturing CO₂ from flue gas in a PSA process.³¹ In their work, they proposed the optimization of the following adsorbent evaluation criteria to examine and rank the performance of the materials at the regeneration condi-

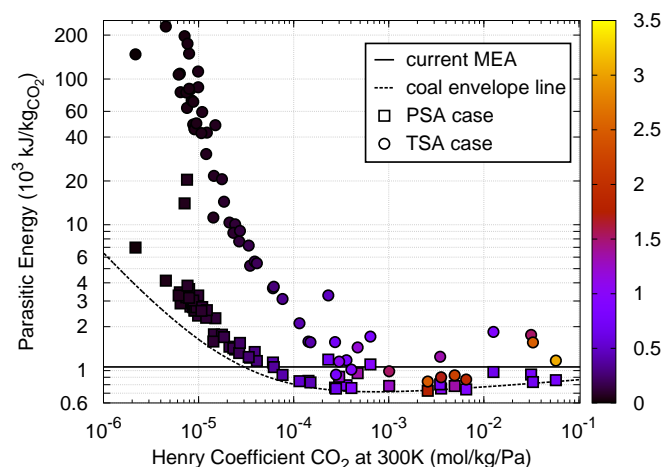


Fig. 7 Parasitic energy based on PSA/TSA and corresponding working capacity. Working capacity is illustrated as a color code in mol/kg.

tions $T_{\text{ads/des}} = 298$ K, $p_{\text{ads}} = 1$ bar and $p_{\text{des}} = 0.1$ bar and a CO₂:N₂ gas composition of 90 : 10.

- CO₂ uptake ($q_{\text{CO}_2}^{\text{ads}}$)
- adsorption selectivity* $\alpha_{\text{CO}_2, \text{N}_2}^{\text{ads}} = (q_{\text{CO}_2}^{\text{ads}}/q_{\text{N}_2}^{\text{ads}}) \cdot (y_{\text{N}_2}/y_{\text{CO}_2})$
- working capacity $\Delta q_{\text{CO}_2} = q_{\text{CO}_2}^{\text{ads}} - q_{\text{CO}_2}^{\text{des}}$
- regenerability† $R = (\Delta q_{\text{CO}_2}/q_{\text{CO}_2}^{\text{ads}})$
- sorbent selection parameter $S = (\alpha_{\text{CO}_2, \text{N}_2}^{\text{ads}})^2 / \alpha_{\text{CO}_2, \text{N}_2}^{\text{des}} \cdot \Delta q_{\text{CO}_2} / \Delta q_{\text{N}_2}$
- CO₂ heat of adsorption Δh_{CO_2}

Note that the sorbent selection parameter is a combination of two separate criteria. The first part expresses the importance of the selectivities during adsorption and desorption.⁷⁴ The second term represents the fraction of the working capacities.^{75,76} Both criteria together are used to facilitate the performance assessment and to improve the classification of the materials.³¹

A recent perspective³⁰ on MOFs for CO₂ capture and separation by Zhang et al. also highlighted four of the above mentioned criteria, namely capacity, selectivity, regeneration, and heat of adsorption, as crucial ones to evaluate solid adsorbents for use in the CO₂ capture and separation process.

As the parasitic energy is a weighted overall property, it is instructive to see how the above criteria contribute to the parasitic energy. Unlike Bae et al., we considered a flue gas composition of 14 : 86 (CO₂:N₂) at adsorption conditions of $T_{\text{ads}} = 313$ K and $p_{\text{ads}} = 1$ atm. For regeneration, the capture gas composition was set to 99 : 1 (CO₂:N₂) with desorption

* $y_{\text{CO}_2, \text{N}_2}$ denote the molar CO₂ and N₂ fractions in the gas phase, respectively
 † fraction of adsorption sites released during desorption.⁷³

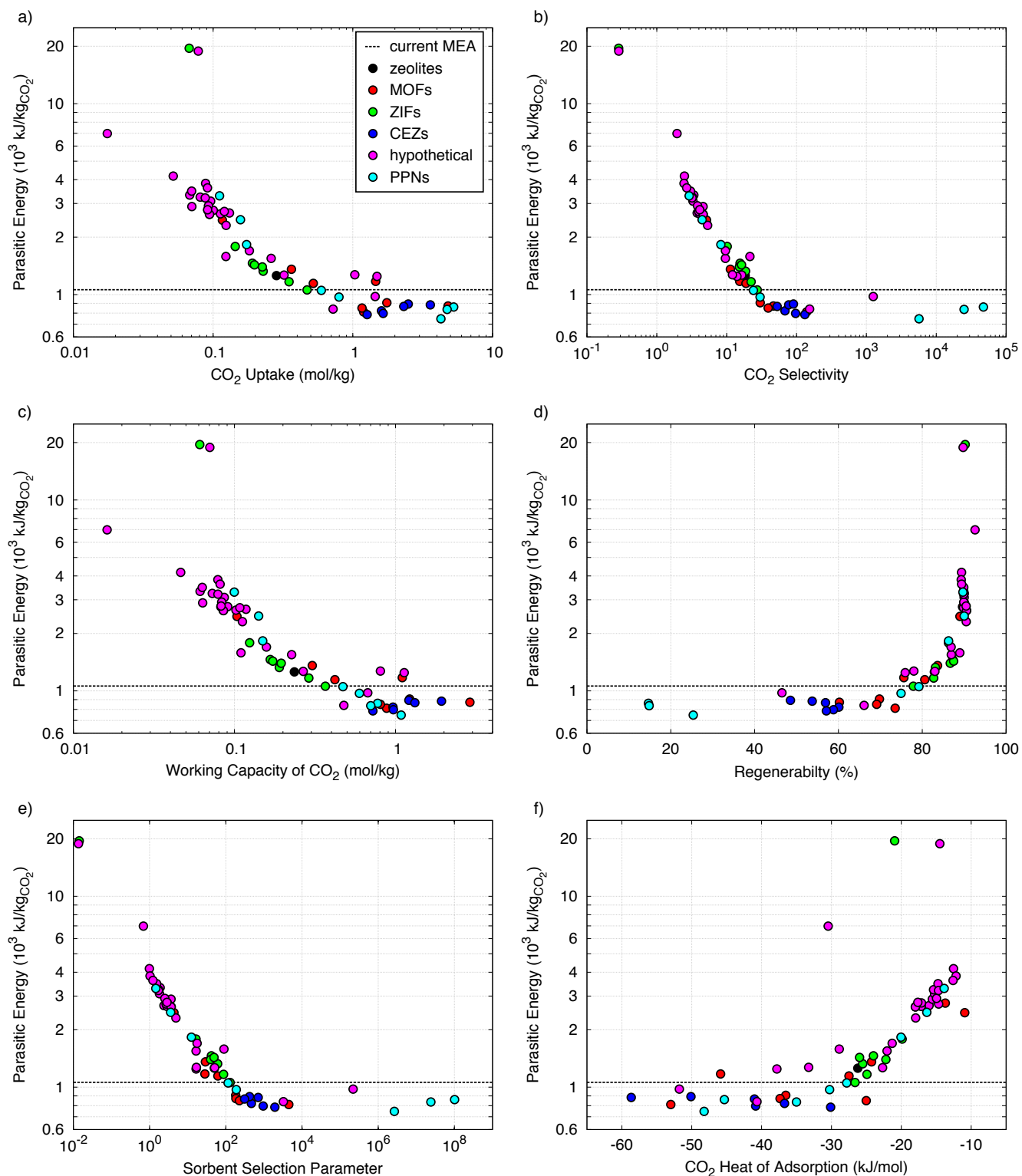


Fig. 8 Comparison of parasitic energy and other evaluation criteria. Parasitic energy is shown as function of the different evaluation criteria.

conditions (T_{des} and p_{des}) optimized according to the minimal parasitic energy. The same conditions were applied for the calculation of the evaluation criteria. Both, parasitic energy and the proposed evaluation criteria are based on the competitive Langmuir model to avoid limitations of IAST at very high differences in Henry coefficients of adsorbed components.

Figure 8 compares our parasitic energy with the different criteria. Figure 8-(a) depicts the parasitic energy as a function of the CO₂ uptake. Small CO₂ uptakes require the entire column to be brought to desorption conditions which causes high parasitic energies with only a small amount of CO₂ being removed. We see a monotonic decrease of the parasitic energy towards higher CO₂ uptakes. However, for materials with a CO₂ uptake higher than 0.7 mol/kg, the parasitic energy does not decrease further. Materials with a very high uptake could be more difficult to regenerate which is why the reduction in parasitic energy with increasing CO₂ uptake is compensated by increasing regeneration costs.

A similar trend is observed for the CO₂ selectivity in figure 8-(b). Materials with a higher selectivity will have a lower parasitic energy. The higher the selectivity, the lower the compression costs for the captured gas as it will contain less N₂. However, if the selectivity increases above 10², the gain in selectivity is compensated by higher regeneration costs.

As the working capacity is closely related to the maximum uptake, we observe a similar trend in figure 8-(c): the parasitic energy decreases with increasing working capacity but above a capacity of (0.7 mol/kg) the parasitic energy does not improve further.

Figure 8-(d) presents the parasitic energy dependency on material regenerability. Materials with low parasitic energy requirements regenerate worse than materials with high parasitic energies. Materials below the MEA performance line feature regenerabilities of 15 – 70%, whereas materials above it regenerate beyond 80%. Regenerability is defined as the fraction of working capacity (equivalent to produced amount of CO₂) and uptake (actually captured amount of CO₂). Materials with only little, weak or not selective binding sites regenerate easily, *i.e.* close to 100%, since little CO₂ was adsorbed to start with and almost all of it desorbed. Contrary, materials with low parasitic energies firstly exhibit strong or highly selective binding sites and secondly possess a lot of them. Thus, low regenerability denotes that a relatively small amount of CO₂ was produced compared to the present binding sites. Clearly, regenerability is not a criterion we can use in isolation.

Figure 8-(e) shows the parasitic energy as a function of the sorbent selection parameter. Similar to uptake and working capacity, the results bear resemblance to the selectivity dependence in plot 8-(b). Both criteria yield in the same ranking results, merely the sorbent selection parameter axis seems to be stretched compared to selectivity. The sorbent selection parameter can be expressed by the selectivity with a non-

constant exponent. Hence, this criterion magnifies selectivity differences between materials.

The last plot in figure 8 displays the correlation between parasitic energy and the CO₂ heat of adsorption. In general, approaching more negative heat of adsorption values result in lower, more promising parasitic energies. Materials possessing Δh values higher than about –25 kJ/mol are generally located above the current amine-scrubbing performance line. Whereas Δh values lower than about –30 kJ/mol mostly lead to well performing materials. Figure 8-(f), however, also does not highlight any optimum heat of adsorption which would justify optimizing this criterion. Hence, Δh as a single criterion is likewise not suited to determine promising materials but serves as an indicator for low parasitic energies.

Summarizing the results gathered from figure 8 yields in the following conclusions. Only four of the six presented evaluation criteria are real independent criteria. Applying the criteria individually does give important insights but does not reveal the optimal material. The combination of the proposed evaluation criteria is therefore a necessity as was also pointed out by Bae et al. ³¹

5 Carbon capture at low concentrations

The CO₂ concentration in the exhaust gases of power plants can be variable. Herein, it is interesting to see how the selection of the optimal material depends on the source of the flue gas. In this section, we look at carbon capture from natural gas and capture directly from air.

5.1 Carbon capture of natural gas

We can also screen the different materials to capture carbon from flue gas of a natural gas fired power plant. For a typical gas fired power plant the CO₂ concentration in flue gas is ca. 4%. Figure 9 shows the parasitic energy results for natural gas as a function of the CO₂ Henry coefficient (k_{H,CO_2}) at 300 K. The shape of the curve is similar to the one for flue gas of a coal fired power plant which was shown in subsection 4.1. However, the optimal Henry coefficient region is shifted to higher values and now at 10⁻³ – 10⁻¹ mol/kgPa compared to 10⁻⁴ – 10⁻² mol/kgPa for coal flue gas. Furthermore, figure 9 shows that the parasitic energies for flue gas of natural gas are higher compared to results predicted for a coal-fired power plant.

As the CO₂ concentration in flue gas from natural gas is lower compared to flue gas from coal, a stronger interaction with CO₂ is needed to reach the same working capacities. However, a stronger CO₂ interaction also implies that the regeneration costs will increase. Consequently, the lowest reached parasitic energies are higher than in case of coal. For very high Henry coefficient values, though, the materials will

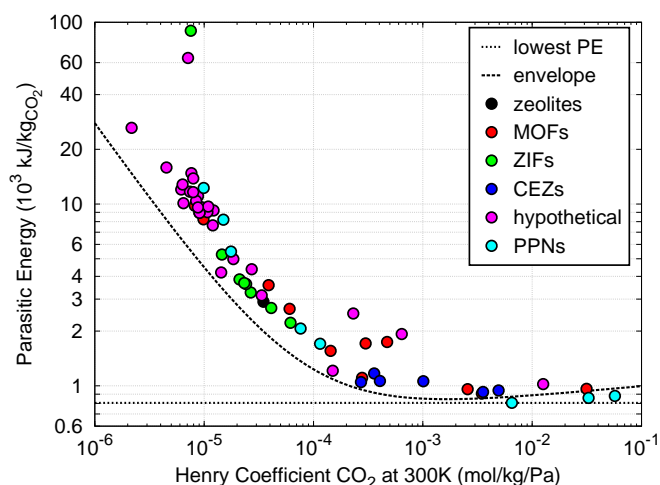


Fig. 9 Characteristic plot of parasitic energy for natural gas. Dashed line indicates envelope for natural gas based on a large library of hypothetical zeolites. Further details on the envelope can be found in the supporting information. The lowest parasitic energy is predicted for PPN-6-CH₂TETA at 806.53 kJ/kgCO₂.

be close to saturation, and the working capacity will hence be less sensitive to the initial CO₂ concentration in the flue gas. This results in a similar parasitic energy for flue gas from natural gas and coal.

In our screening, the best material for natural gas carbon capture is the amine-functionalized PPN-6-CH₂TETA with a parasitic energy of 806.53 kJ/kgCO₂. For coal we found Mg-MOF-74 to be the best performing material. For natural gas, however, this MOF exhibits a parasitic energy of 958.68 kJ/kgCO₂ which is even higher than the other analyzed amine-functionalized PPN-6 materials and the zinc centered SIFSIX-3-M (PPN-6CH₂TAEA < PPN-6-CH₂DETA < SIFSIX-3-Zn < Mg-MOF-74). A selection of materials with corresponding parasitic energies is shown in Table 4.

Table 4 Selection of materials with the lowest parasitic energy results (in kJ/kgCO₂) for natural gas (CO₂ : N₂ = 4 : 96), sorted by decreasing performance.

material	PE	material	PE
PPN-6-CH ₂ TETA	807	SIFSIX-3-Cu	963
PPN-6-CH ₂ TAEA	858	ZIF-36-CAG	1,022
PPN-6-CH ₂ DETA	880	NaA	1,048
SIFSIX-3-Zn	907	CaX	1,060
NaX	925	MgX	1,063
CaA	943	mnen-CuBTTri	1,106
Mg-MOF-74	959	MgA	1,170

In general, the parasitic energy results indicate that applying CCS on natural gas based flue gas puts a higher addi-

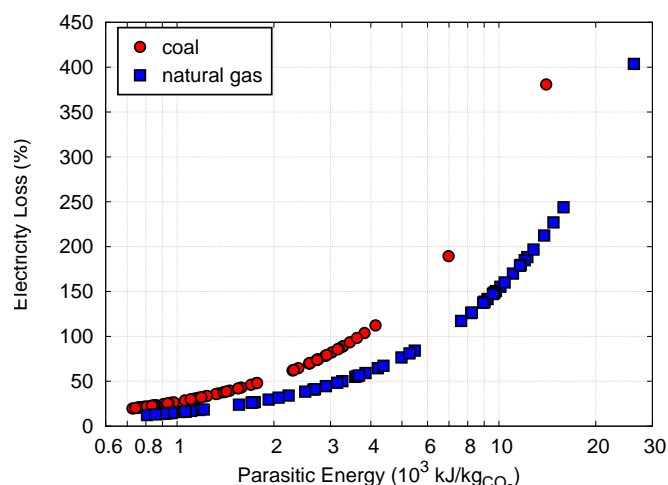


Fig. 10 Electricity loss comparison between coal-fired and natural gas-fired power plants. Electricity loss is shown as a function of the parasitic energy.

tional energy load per kg captured CO₂ on a power plant than coal flue gas. This does not imply that the total energy loss of carbon capture for natural gas is also higher. Natural gas fired power plants produce less carbon for the same electricity output.⁷⁷ Compared to coal, natural gas is known to produce twice as much electricity based on the amount CO₂ produced (1842 kWh/t_{coal} and 127 kWh/Mcf_{natural gas}, respectively).⁷⁸ Based on these values provided by the U.S. Energy Information Administration we computed the total energy loss by parasitic energy for both gas compositions (see supporting information). Figure 10 illustrates the energy loss in terms of electricity caused by applying CCS in coal and natural gas power plants as function of the parasitic energy requirement on a material-by-material basis. Even though we can find materials for carbon capture from coal fired power plants with a lower parasitic energy compared to natural gas flue gas, the overall loss in electric energy for natural gas is smaller (10 – 20%) compared to coal (20 – 30%).

5.2 Carbon capture directly from air

Until now, we studied the parasitic energy of CCS with respect to the capture of CO₂ at its place of origin in the power plant. In the following, we instead look into CO₂ capture directly from air. We ask if this could provide a valuable alternative for the power plant to make up for its CO₂ emissions by "recapturing" the same amount from the atmosphere.⁷⁹ A CCS unit operated in this manner would also be powered by the heat and electricity from the power plant, of course.

Figure 11 shows the parasitic energy of direct air capture as a function of the Henry coefficient of CO₂ at 300 K and compares it to those of coal and natural gas. In this calculation, we

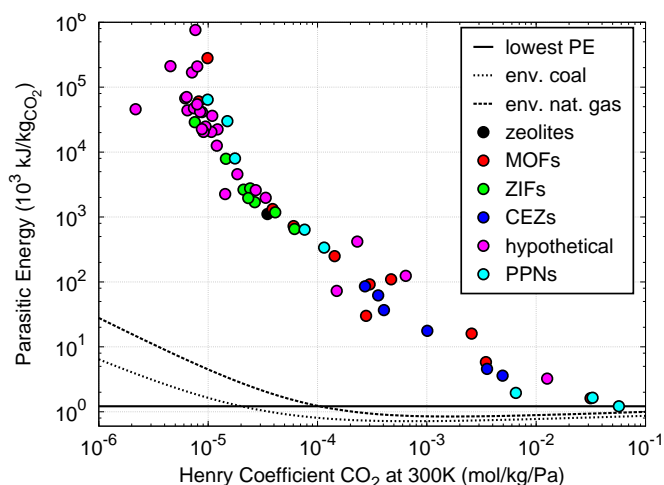


Fig. 11 Characteristic plot of parasitic energy for direct air capture. Solid and dashed lines show envelopes for coal and natural gas, respectively. Best performing materials for air capture is PPN-6-CH₂DETA: 1,214.62 kJ/kgCO₂.

assumed an average CO₂ concentration in the atmosphere of 400 ppm.⁷⁹ We see that the optimal materials have the highest Henry coefficients which is consistent with the trend we saw for natural gas. Moreover, the effect of the flue gas composition on the parasitic energy becomes less important for these high Henry coefficients as the results steadily approach the coal and natural gas values.

The best performing material for direct air capture is the amine-functionalized PPN-6-CH₂DETA with a parasitic energy of 1,215 kJ/kgCO₂ which corresponds to an electricity loss of 33% in a coal fired power plant. This value is almost twice as high as the result for the corresponding optimal material for coal flue gas capture (727 kJ/kgCO₂, 20% electricity loss). In comparison to natural gas, the series of amine-functionalized PPN-6 materials has inverted the performance order (PPN-6-CH₂DETA < PPN-6-CH₂TAEA < PPN-6-CH₂TETA). An identical behavior is also observed in the series of SIFSIX-3-M. In coal and natural gas separation, SIFSIX-3-Zn outperforms SIFSIX-3-Cu. For direct air capture, however, SIFSIX-3-Cu was identified as the second best performing material within all materials under investigation (1,617 kJ/kgCO₂). Thus, SIFSIX-3-Cu is well suited for this kind of separation process as was also highlighted by Shekhah et al. . While the parasitic energies of the above PPN and SIFSIX-3-M classes are relatively close to each other, the value of Mg-MOF-74, the best performing material for coal flue gas separation, is already an order of magnitude larger (16 MJ/kgCO₂). A selection of materials with corresponding parasitic energies is shown in Table 5.

Figure 11 also shows that the optimal Henry coefficient region is not reached by the materials we have studied. Materials

Table 5 Selection of materials with the lowest parasitic energy results (in kJ/kgCO₂) for direct air capture (CO₂ concentration: 400 ppm), sorted by decreasing performance.

material	PE	material	PE
PPN-6-CH ₂ DETA	1,215	SIFSIX-3-Zn	5,809
SIFSIX-3-Cu	1,617	Mg-MOF-74	16,003
PPN-6-CH ₂ TAEA	1,645	CaX	17,642
PPN-6-CH ₂ TETA	1,948	mmen-CuBTTri	30,028
ZIF-36-CAG	3,240	MgX	36,825
CaA	3,595	MgA	62,012
NaX	4,570	ZIF-36-FRL	72,649

with even higher Henry coefficients might give lower parasitic energies closer to the results of coal and natural gas.

6 Conclusion and Outlook

We have predicted the performance for over 60 synthesized and hypothetical nano-porous materials on the basis of experimental and simulated data using the new approach of parasitic energy. Parasitic energy has identified Mg-MOF-74, PPN-6-CH₂TETA, and PPN-6-CH₂DETA as the most promising materials for CCS in coal, natural gas, and direct air capture, respectively. The low CO₂ concentrations in the latter two always result in higher parasitic energies compared to coal. Despite the increased energy requirements, natural gas, however, produces three times more electricity which yields in an overall smaller electricity loss. Our work also revealed that implementing different regeneration strategies affects the parasitic energy predictions enormously. All materials exhibit higher parasitic energy values when applying TSA for desorption, while PSA and TPSA result in approximately identical low parasitic energy predictions. Additionally, we compared the concept of parasitic energy to the theoretical minimal energy penalty for simply separating an ideal gas mixture and further also to other proposed evaluation criteria to evaluate their ability to rank materials and to point out prediction differences. The results have shown that parasitic energy is a suitable metric to evaluate materials for CCS without further consideration of additional criteria. Parasitic energy not only includes the energy estimation for the compression process which is completely neglected in other ranking methods and plays a crucial part in the total energy penalty, but also combines several essential thermodynamic properties. Consequently, the parasitic energy model is a well suited metric for high-throughput screening of large databases.

Quite remarkably, none of the various experimental structures perform better in parasitic energy than the according prediction by the best zeolite structures (dashed line in fig-

ure 4). This observation is probably related to the creation and amount of binding sites regardless of the specific material class. The best materials not only exhibit the maximum number of sites best suited for CO₂ adsorption, but also a similar minimum number of material atoms needed to create an optimal binding site. The minimum volume required for a single CO₂ adsorption is defined by the CO₂ molecule and the minimal number of atoms for the binding site. As this volume represents the minimum involved in a CCS process we do not expect materials to perform better than the zeolite line.

To give chemists and material scientists guidelines in the pursuit of new, more efficient nano-porous materials for CCS on the basis of parasitic energy, we conclude that selectively improving a particular material property does not ensure a superior performance in terms of energetic costs. Instead, a careful consideration of the interplay between various materials properties (*e.g.*, uptake, selectivity, working capacity, and regeneration) can potentially lead to lower parasitic energies. Note that the working capacity reached in a PSA process is of less importance compared to the selectivity, uptake, and consequently Henry coefficient (see 4.2). We anticipate that an additional reduction of the energy cost can be achieved at least for natural gas separation and direct air capture. For coal, we are, however, not expecting any further significant improvements as pointed out in the previous paragraph.

It should be noted, that the approach of parasitic energy only provides the energy requirement which is needed to capture one kilogram of CO₂ and does not give information on the total amount of captured CO₂. Furthermore, no approximation on the investment costs for the adsorbents or retrofitting the facilities are included. It also needs to be mentioned that the shown results represent the material evaluation for CCS on the basis of a two-component flue gas, merely considering CO₂ and N₂. In reality, power plant flue gas exhibits several additional components, like SO_x, NO_x, and water in significant amounts (5-15 vol%).⁸⁰ Water is known to compete strongly for the CO₂ adsorption sites.⁸¹⁻⁸⁵ This characteristic could modify the current material ranking completely. Hence, further investigations need to be conducted to get a more reliable parasitic energy prediction for real flue gas conditions.

Acknowledgements

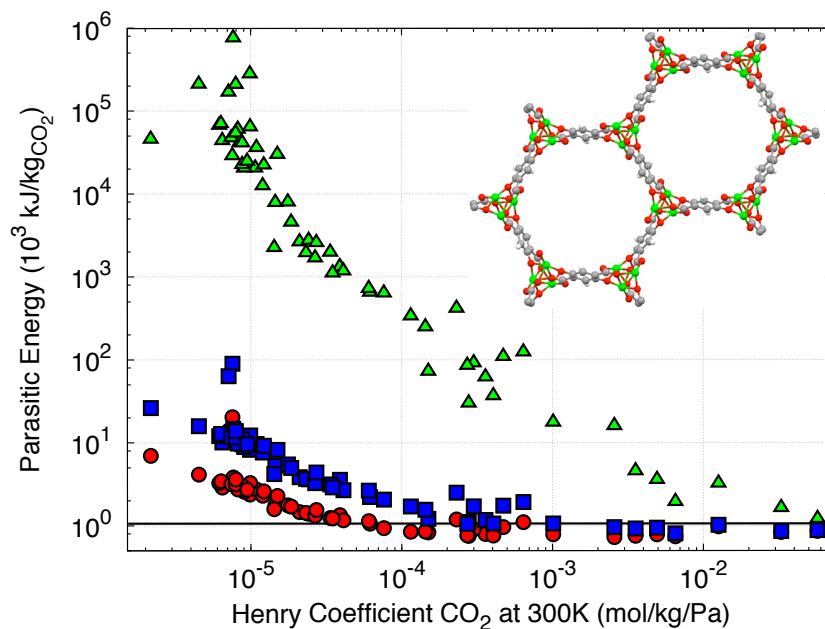
This work was supported by the Center for Gas Separations Relevant to Clean Energy Technologies, an Energy Frontier Research Center funded by the U.S. Department of Energy, Office of Science, Office of Basic Energy Sciences, under Award Number DE-SC0001015.

References

- 1 B. Smit, J. R. Reimer, C. M. Oldenburg and I. C. I. C. Bourg, *Introduction to Carbon Capture and Sequestration*, Imperial College Press, London, 1st edn., 2014.
- 2 M. M. F. Hasan, E. L. First and C. A. Floudas, *Physical chemistry chemical physics : PCCP*, 2013, **15**, 17601–18.
- 3 S. Keskin, T. M. van Heest and D. S. Sholl, *ChemSusChem*, 2010, **3**, 879–91.
- 4 R. H. Socolow, *Scientific American*, 2006, **295**, 2006.
- 5 *Fourth Assessment Report: Mitigation of Climate Change*, 2007, http://www.ipcc.ch/publications_and_data/ar4/wg3/en/ch4s4-3-1.html.
- 6 J. Wilcox, *Carbon Capture*, Springer, New York, 1st edn., 2012.
- 7 J. P. Ciferno, J. J. Marano and R. K. Munson, *CHEMICAL ENGINEERING PROGRESS*, 2011, **107**, 34–44.
- 8 R. Bottoms, *Separating acid gases*, 1930.
- 9 G. Rochelle, E. Chen, S. Freeman, D. Van Wagener, Q. Xu and A. Voice, *Chemical Engineering Journal*, 2011, **171**, 725–733.
- 10 G. T. Rochelle, *Science (New York, N.Y.)*, 2009, **325**, 1652–4.
- 11 A. S. Bhowan and B. C. Freeman, *Environmental science & technology*, 2011, **45**, 8624–32.
- 12 T. C. Merkel, H. Lin, X. Wei and R. Baker, *Journal of Membrane Science*, 2010, **359**, 126–139.
- 13 R. P. Lively, R. R. Chance, J. A. Mysona, V. P. Babu, H. W. Deckman, D. P. Leta, H. Thomann and W. J. Koros, *International Journal of Greenhouse Gas Control*, 2012, **10**, 285–294.
- 14 R. P. Lively, M. E. Dose, L. Xu, J. T. Vaughn, J. Johnson, J. A. Thompson, K. Zhang, M. E. Lydon, J.-S. Lee, L. Liu, Z. Hu, O. Karvan, M. J. Realff and W. J. Koros, *Journal of Membrane Science*, 2012, **423-424**, 302–313.
- 15 Y. Dai, J. Johnson, O. Karvan, D. S. Sholl and W. Koros, *Journal of Membrane Science*, 2012, **401-402**, 76–82.
- 16 R. Adams, C. Carson, J. Ward, R. Tannenbaum and W. Koros, *Microporous and Mesoporous Materials*, 2010, **131**, 13–20.
- 17 T.-H. Bae and J. R. Long, *Energy & Environmental Science*, 2013, **6**, 3565.
- 18 D. Luebke, C. Myers and H. Pennline, *Energy & Fuels*, 2006, **20**, 1906–1913.
- 19 J. Kim, M. Abouelnasr, L.-C. Lin and B. Smit, *Journal of the American Chemical Society*, 2013, **135**, 7545–52.
- 20 D. M. D'Alessandro, B. Smit and J. R. Long, *Angewandte Chemie (International ed. in English)*, 2010, **49**, 6058–82.
- 21 K. Sumida, D. L. Rogow, J. A. Mason, T. M. McDonald, E. D. Bloch, Z. R. Herm, T.-H. Bae and J. R. Long, *Chemical reviews*, 2012, **112**, 724–81.
- 22 J.-R. Li, J. Sculley and H.-C. Zhou, *Chemical reviews*, 2012, **112**, 869–932.
- 23 M. W. Deem, R. Pophale, P. A. Cheeseman and D. J. Earl, *The Journal of Physical Chemistry C*, 2009, **113**, 21353–21360.
- 24 R. Banerjee, A. Phan, B. Wang, C. Knobler, H. Furukawa, M. O'Keeffe and O. M. Yaghi, *Science (New York, N.Y.)*, 2008, **319**, 939–43.
- 25 W. Lu, D. Yuan, D. Zhao, C. I. Schilling, O. Pietzsch, T. Muller, S. Brase, J. Guenther, J. Blumel, R. Krishna, Z. Li and H.-C. Zhou, *Chemistry of Materials*, 2010, **22**, 5964–5972.
- 26 H. Furukawa, K. E. Cordova, M. O'Keeffe and O. M. Yaghi, *Science (New York, N.Y.)*, 2013, **341**, 1230444.
- 27 S. Ziaii, G. T. Rochelle and T. F. Edgar, *Industrial & Engineering Chemistry Research*, 2009, **48**, 6105–6111.
- 28 J. P. Sculley, W. M. Verdegaal, W. Lu, M. Wriedt and H.-C. Zhou, *Advanced materials (Deerfield Beach, Fla.)*, 2013, **25**, 3957–61.
- 29 A. D. Wiersum, J.-S. Chang, C. Serre and P. L. Llewellyn, *Langmuir : the ACS journal of surfaces and colloids*, 2013, **29**, 3301–9.
- 30 Z. Zhang, Z.-Z. Yao, S. Xiang and B. Chen, *Energy & Environmental*

- Science*, 2014, **7**, 2868.
- 31 Y.-S. Bae and R. Q. Snurr, *Angewandte Chemie (International ed. in English)*, 2011, **50**, 11586–96.
 - 32 R. Krishna and J. M. van Baten, *Physical chemistry chemical physics : PCCP*, 2011, **13**, 10593–616.
 - 33 R. Krishna and J. R. Long, *The Journal of Physical Chemistry C*, 2011, **115**, 12941–12950.
 - 34 J. M. Simmons, H. Wu, W. Zhou and T. Yildirim, *Energy & Environmental Science*, 2011, **4**, 2177.
 - 35 A. O. Yazaydin, R. Q. Snurr, T.-H. Park, K. Koh, J. Liu, M. D. Levan, A. I. Benin, P. Jakubczak, M. Lanuza, D. B. Galloway, J. J. Low and R. R. Willis, *Journal of the American Chemical Society*, 2009, **131**, 18198–9.
 - 36 R. Banerjee, H. Furukawa, D. Britt, C. Knobler, M. O’Keeffe and O. M. Yaghi, *Journal of the American Chemical Society*, 2009, **131**, 3875–7.
 - 37 *NIST Reference Fluid Thermodynamic and Transport Properties Database (REFPROP): Version 9.0.*, 2010, <http://www.nist.gov/srd/nist23.cfm>.
 - 38 *The GERG-2004 Wide-Range Equation of State for Natural Gases and Other Mixtures (GERG TM15)*, 2007, http://www.gerg.eu/public/uploads/files/publications/technical_monographs/tm15_04.pdf.
 - 39 T. Dixon, K. Yamaji, A. H. Berger and A. S. Bhowan, *Energy Procedia*, 2013, **37**, 25–32.
 - 40 S. A. Freeman, R. Dugas, D. H. Van Wagener, T. Nguyen and G. T. Rochelle, *International Journal of Greenhouse Gas Control*, 2010, **4**, 119–124.
 - 41 *Carbon Dioxide Capture from Existing Coal-Fired Power Plants*, 2007, <http://www.netl.doe.gov/File%20Library/Research/Energy%20Analysis/Publications/CO2-Retrofit-From-Existing-Plants-Revised-November-2007.pdf>.
 - 42 A. L. Myers and J. M. Prausnitz, *AIChE Journal*, 1965, **11**, 121–127.
 - 43 M. B. Rao and S. Sircar, *Langmuir*, 1999, **15**, 7258–7267.
 - 44 P. M. Piccione, B. F. Woodfield, J. Boerio-Goates, A. Navrotsky and M. E. Davis, *The Journal of Physical Chemistry B*, 2001, **105**, 6025–6030.
 - 45 P. Vieillard, *European Journal of Mineralogy*, 2010, **22**, 823–836.
 - 46 B. Mu and K. S. Walton, *The Journal of Physical Chemistry C*, 2011, **115**, 22748–22754.
 - 47 X.-C. Lv, Z.-C. Tan, X.-H. Gao, Z.-H. Zhang, L.-N. Yang, J.-N. Zhao, L.-X. Sun and T. Zhang, *Thermochimica Acta*, 2006, **450**, 102–104.
 - 48 H. Arrouche, S. Aguado, J. Pérez-Pellitero, C. Chizallet, F. Siperstein, D. Farrusseng, N. Bats and C. Nieto-Draghi, *The Journal of Physical Chemistry C*, 2011, **115**, 16425–16432.
 - 49 H. Huang, W. Zhang, D. Liu, B. Liu, G. Chen and C. Zhong, *Chemical Engineering Science*, 2011, **66**, 6297–6305.
 - 50 T.-H. Bae, M. R. Hudson, J. A. Mason, W. L. Queen, J. J. Dutton, K. Sumida, K. J. Micklash, S. S. Kaye, C. M. Brown and J. R. Long, *Energy & Environmental Science*, 2013, **6**, 128.
 - 51 W. Lu, D. Yuan, J. Sculley, D. Zhao, R. Krishna and H.-C. Zhou, *Journal of the American Chemical Society*, 2011, **133**, 18126–9.
 - 52 D. Yuan, W. Lu, D. Zhao and H.-C. Zhou, *Advanced materials (Deerfield Beach, Fla.)*, 2011, **23**, 3723–5.
 - 53 J. A. Mason, K. Sumida, Z. R. Herm, R. Krishna and J. R. Long, *Energy & Environmental Science*, 2011, **4**, 3030.
 - 54 T. M. McDonald, D. M. D’Alessandro, R. Krishna and J. R. Long, *Chemical Science*, 2011, **2**, 2022.
 - 55 P. Aprea, D. Caputo, N. Gargiulo, F. Iucolano and F. Pepe, *Journal of Chemical & Engineering Data*, 2010, **55**, 3655–3661.
 - 56 P. Chowdhury, S. Mekala, F. Dreisbach and S. Gumma, *Microporous and Mesoporous Materials*, 2012, **152**, 246–252.
 - 57 P. D. C. Dietzel, R. Blom and H. Fjellvåg, *European Journal of Inorganic Chemistry*, 2008, **2008**, 3624–3632.
 - 58 P. D. C. Dietzel, V. Besikiotis and R. Blom, *Journal of Materials Chemistry*, 2009, **19**, 7362.
 - 59 L. Grajciar, A. D. Wiersum, P. L. Llewellyn, J.-S. Chang and P. Nachtigall, *The Journal of Physical Chemistry C*, 2011, **115**, 17925–17933.
 - 60 Z. Liang, M. Marshall and A. L. Chaffee, *Energy & Fuels*, 2009, **23**, 2785–2789.
 - 61 B. Mu, P. M. Schoenecker and K. S. Walton, *The Journal of Physical Chemistry C*, 2010, **114**, 6464–6471.
 - 62 K. Uemura, A. Maeda, T. K. Maji, P. Kanoo and H. Kita, *European Journal of Inorganic Chemistry*, 2009, **2009**, 2329–2337.
 - 63 P. Nugent, Y. Belmabkhout, S. D. Burd, A. J. Cairns, R. Luebke, K. Forrest, T. Pham, S. Ma, B. Space, L. Wojtas, M. Eddaoudi and M. J. Zaworotko, *Nature*, 2013, **495**, 80–4.
 - 64 O. Shekhah, Y. Belmabkhout, Z. Chen, V. Guillerm, A. Cairns, K. Adil and M. Eddaoudi, *Nature communications*, 2014, **5**, 4228.
 - 65 Z. R. Herm, J. A. Swisher, B. Smit, R. Krishna and J. R. Long, *Journal of the American Chemical Society*, 2011, **133**, 5664–7.
 - 66 W. Lu, J. P. Sculley, D. Yuan, R. Krishna, Z. Wei and H.-C. Zhou, *Angewandte Chemie (International ed. in English)*, 2012, **51**, 7480–4.
 - 67 Y.-S. Bae, O. K. Farha, A. M. Spokoyny, C. A. Mirkin, J. T. Hupp and R. Q. Snurr, *Chemical communications (Cambridge, England)*, 2008, 4135–7.
 - 68 J. W. Yoon, Y.-K. Seo, Y. K. Hwang, J.-S. Chang, H. Leclerc, S. Wutke, P. Bazin, A. Vimont, M. Daturi, E. Bloch, P. L. Llewellyn, C. Serre, P. Horcajada, J.-M. Grenèche, A. E. Rodrigues and G. Férey, *Angewandte Chemie (International ed. in English)*, 2010, **49**, 5949–52.
 - 69 J. Liu, P. K. Thallapally, B. P. McGrail, D. R. Brown and J. Liu, *Chemical Society reviews*, 2012, **41**, 2308–22.
 - 70 S. R. Caskey, A. G. Wong-Foy and A. J. Matzger, *Journal of the American Chemical Society*, 2008, **130**, 10870–1.
 - 71 R. L. Martin, L.-C. Lin, K. Jariwala, B. Smit and M. Haranczyk, *The Journal of Physical Chemistry C*, 2013, **117**, 12159–12167.
 - 72 L.-C. Lin, A. H. Berger, R. L. Martin, J. Kim, J. A. Swisher, K. Jariwala, C. H. Rycroft, A. S. Bhowan, M. W. Deem, M. Haranczyk and B. Smit, *Nature materials*, 2012, **11**, 633–41.
 - 73 M. Palomino, A. Corma, F. Rey and S. Valencia, *Langmuir : the ACS journal of surfaces and colloids*, 2010, **26**, 1910–7.
 - 74 F. Notaro, J. T. Mullhaupt, F. W. Leavitt and M. W. Ackley, *US Patent 5,810,909*, 1998.
 - 75 S. Rege and R. Yang, *Separation Science and Technology*, 2001, **36**, 3355–3365.
 - 76 R. T. Yang, *Adsorbents: Fundamentals and Applications*, Wiley, Hoboken, 1st edn., 2003.
 - 77 *How much carbon dioxide (CO₂) is produced per kilowatt-hour when generating electricity with fossil fuels? (EIA, Jan. 2014)*, <http://www.eia.gov/tools/faqs/faq.cfm?id=74&t=11>.
 - 78 *How much coal, natural gas, or petroleum is used to generate a kilowatt-hour of electricity? (EIA, Jan. 2014)*, <http://www.eia.gov/tools/faqs/faq.cfm?id=667&t=2>.
 - 79 *Direct Air Capture of CO₂ with Chemicals*, 2011, <http://www.aps.org/policy/reports/assessments/upload/dac2011.pdf>.
 - 80 *Cost and Performance Baseline for Fossil Energy Plants*, 2010, http://netl.doe.gov/File%20Library/Research/Energy%20Analysis/OE/BitBase_FinRep_Rev2a-3_20130919.1.pdf.
 - 81 Y. Wang and M. D. LeVan, *Journal of Chemical & Engineering Data*, 2009, **54**, 2839–2844.
 - 82 Y. Wang and M. D. LeVan, *Journal of Chemical & Engineering Data*, 2010, **55**, 3189–3195.
 - 83 J. Liu, Y. Wang, A. I. Benin, P. Jakubczak, R. R. Willis and M. D. LeVan, *Langmuir : the ACS journal of surfaces and colloids*, 2010, **26**, 14301–7.
 - 84 L. Joos, J. A. Swisher and B. Smit, *Langmuir : the ACS journal of surfaces and colloids*, 2013, **29**, 15936–42.
 - 85 L.-C. Lin, K. Lee, L. Gagliardi, J. B. Neaton and B. Smit, *Journal of Chemical Theory and Computation*, 2014, **10**, 1477–1488.

In this work, we screen a wide selection of nano-porous materials (i.e. MOFs, zeolites, PPNs, ZIFs, CEZs) with respect to CO₂ adsorption from a bi-component ideal flue gas. As metric we employ the concept of parasitic energy which comprises the entire CCS process. In this context, we also study the impact of various flue gas compositions and regeneration strategies on the material rankings and compare the results to single-property evaluation criteria proposed in literature.



Supporting Information:
Evaluating different classes of porous materials for carbon capture

Johanna M. Huck^{1,2}, Li-Chiang Lin¹, Adam H. Berger³, Mahdi Niknam Sharak^{1,4}, Richard L. Martin⁵, Abhoyjit S. Bhowan³, Maciej Haranczyk⁵, Karsten Reuter², and Berend Smit^{1,6,7}

¹*Dept. of Chemical and Biomolecular Engineering, University of California, Berkeley, CA 94720*

²*Chair for Theoretical Chemistry and Catalysis Research Center, Technische Universität München, Garching, Germany*

³*Electric Power Research Institute (EPRI), 3420 Hillview Avenue, Palo Alto, CA 94304*

⁴*Department of Chemical Engineering, Quchan University of Advanced Technologies, Quchan, Iran*

⁵*Computational Research Division, Lawrence Berkeley National Laboratory, Berkeley, CA 94720*

⁶*Materials Sciences Division, Lawrence Berkeley National Laboratory, Berkeley, CA 94720*

⁷*Laboratory of molecular simulation, Institut des Sciences et Ingénierie Chimiques, Ecole Polytechnique Fédérale de Lausanne (EPFL), CH-1015 Lausanne, Switzerland*

1 Ideal adsorbed solution theory versus competitive Langmuir adsorption model

For the concept of parasitic energy it is essential to specify the influence of the used mixture model on the energy requirement estimation. Therefore parasitic energy was calculated for all investigated materials by means of predicted mixture isotherms using Ideal Adsorbed Solution Theory (IAST) and competitive model to detect potential differences. Figure 1 illustrates the parasitic energy results using both mixture isotherm predictions. The results of the competitive model are shown as function of the IAST results in a double logarithmic plot. For the majority of materials both models exhibit almost equal parasitic energies. In particular in the higher parasitic energy region, 1000 kJ/kgCO₂ and higher, the IAST results are in good agreement to these of the competitive model as most materials with the exception of a few are located on or close to the diagonal dashed line. These structures, strictly speaking, the synthesized materials PPN-6, PPN-6-CH₂Cl, PPN-6-SO₃H, PPN-6-SO₃Li and the theoretical materials ZIF-40-GIS and ZIF-116-CAG exhibit a quite large CO₂ selectivity in IAST compared to the results from the competitive approach, causing such high differences.

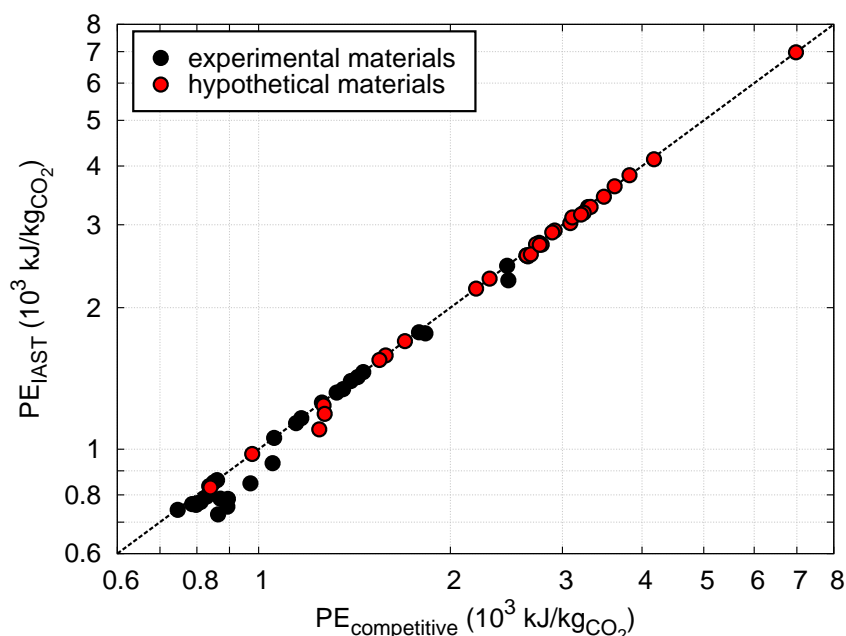


Figure 1: Comparison of IAST and Competitive model based parasitic energies for coal flue gas. Dashed diagonal line illustrates degree of consistency between the results of both models. Results based on experimental data are shown as black circles. Theoretical results are marked as red circles. Mg-MOF-74 exhibits highest parasitic energy difference of $\sim 16\%$ ($PE_{IAST} = 727.12$ kJ/kgCO₂, $PE_{comp} = 863.74$ kJ/kgCO₂).

Examining the significant low parasitic energy region (< 1000 kJ/kgCO₂) also reveals intensified aberrations between the results. The parasitic energy results on the basis of IAST tend to predict lower energy requirements than using the competitive model. Materials that are affected particularly are Mg-MOF-74, mmen-CuBTTri, PPN-6-SO₃H, CaA, CaX and NaX. These discrepancies can be explained by the presence of strong binding sites. All affected materials are known to exhibit strong binding sites like open-metal sites (Mg-MOF-74)¹, extraframework cations (CaA, CaX and NaX)² and additional functional groups (mmen-CuBTTri)³. Due to these strong binding sites IAST predicts a higher CO₂ : N₂ selectivity for these materials and thus higher CO₂ purities. Resulting less compression work is needed to reach the intended pressure of 150 bar for transportation and storage. The metal-organic framework Mg-MOF-74 indicates the largest difference of $\sim 16\%$. Investigating simulated mixture isotherms of coal flue gas in Mg-MOF-74 have shown that the predictions of IAST are in a good agreement.¹ Thus, the parasitic energy results used in the main article are based on the IAST approach for the prediction of the mixture isotherms.

2 Calculating the minimal separation work

The basic equation to estimate the minimum energy ($W_{\text{sep}}^{\text{min}}$) required to separate a two-component gas mixture is given by

$$\begin{aligned} -W_{\text{sep}}^{\text{min}} &= T\Delta S \\ &= n_{\text{em}}T s^{\text{im}}(x_{\text{em}}) + n_{\text{cap}}T s^{\text{im}}(x_{\text{cap}}) - n_{\text{flue}}T s^{\text{im}}(x_{\text{flue}}) \end{aligned} \quad (1)$$

where n_{em} is the number of moles of the emitted gas, n_{cap} is the number of moles of the captured gas, and n_{flue} is the number of moles of the flue gas. Similarly, x_{em} corresponds to the mole fraction of emitted CO_2 , x_{cap} corresponds to the mole fraction of captured CO_2 , and x_{flue} corresponds to the initial mole fraction of CO_2 in the flue gas. Note that all introduced terms are based on the CO_2 concentration of the respective gas. To estimate the correct minimum energy various cases need to be differentiated. Depending on the CO_2 and inert gas composition of the resulting captured and emitted gas stream we need to include or omit different terms in equation (1). In case of complete separation, resulting in pure CO_2 in the captured gas stream and pure inert gas in the emission stream, both particular molar entropies ($s^{\text{im}}(x_{\text{cap}})$ and $s^{\text{im}}(x_{\text{em}})$) do not contribute to the minimum separation energy. The total number of configurations Ω to capture pure CO_2 and emit pure inert gas equals 1, respectively. Accordingly, the contributing entropies $s^{\text{im}}(x_{\text{cap}})$ and $s^{\text{im}}(x_{\text{em}})$ equal 0, due to

$$s^{\text{im}} \propto \ln \Omega \quad (2)$$

Hence, equation (1) reduces to

$$-W_{\text{sep}}^{\text{min}} = -n_{\text{flue}}T s^{\text{im}}(x_{\text{flue}}) \quad (3)$$

On the other hand, if the gas separation is not 100% complete and CO_2 residue is also present in the emitted gas, whereas the captured gas stream contains pure CO_2 , only the molar entropy of x_{cap} needs to be omitted. The molar entropy of x_{em} , however, contributes to the minimum energy and changes equation (1) to

$$-W_{\text{sep}}^{\text{min}} = n_{\text{em}}T s^{\text{im}}(x_{\text{em}}) - n_{\text{flue}}T s^{\text{im}}(x_{\text{flue}}) \quad (4)$$

and vice versa to

$$-W_{\text{sep}}^{\text{min}} = n_{\text{cap}}T s^{\text{im}}(x_{\text{cap}}) - n_{\text{flue}}T s^{\text{im}}(x_{\text{flue}}) \quad (5)$$

in case of emitting pure inert gas, while inert gas residue remain in the captured gas stream.

For the remaining entropies in equations (1), (3)-(5) in case of $x \neq 0, 1$ the individual molar entropies of an ideal two-component gas mixture can generally be derived using correlation (2) and the Stirling approximation

$$\ln N! \approx N \ln N - N$$

which results in

$$s^{\text{im}}(x) = R[x \ln x + (1-x) \ln(1-x)] \quad (6)$$

where R is the gas constant and x corresponds to the corresponding mole fraction. Forming the mass balance for the total gas and the CO_2 proportionate gas, results in the following equations:

$$n_{\text{flue}} = n_{\text{cap}} + n_{\text{em}} \quad (7)$$

$$x_{\text{flue}} n_{\text{flue}} = x_{\text{cap}} n_{\text{cap}} + x_{\text{em}} n_{\text{em}} \quad (8)$$

Using equations (7) and (8) one can determine n_{cap} and n_{em}

$$n_{\text{cap}} = \frac{x_{\text{flue}} - x_{\text{em}}}{x_{\text{cap}} - x_{\text{em}}} n_{\text{flue}} \quad (9)$$

$$n_{\text{em}} = \frac{x_{\text{flue}} - x_{\text{cap}}}{x_{\text{em}} - x_{\text{cap}}} n_{\text{flue}} \quad (10)$$

Furthermore, an additional parameter α can be introduced if one aims for a specific CO_2 capture efficiency. In this case the captured and emitted CO_2 fractions can be expressed as the ratio of the initial CO_2 concentration in the flue gas. Consequently, n_{cap} and n_{em} yield in

$$n_{\text{cap}} = \frac{\alpha x_{\text{flue}}}{x_{\text{cap}}} n_{\text{flue}} \quad (11)$$

$$n_{\text{em}} = \frac{(1-\alpha)x_{\text{flue}}}{x_{\text{em}}} n_{\text{flue}} \quad (12)$$

Usually, variable x_{cap} is known for a specific separation process, as it corresponds to the aimed concentration of captured CO_2 . However, x_{em} needs to be determined by equalizing equation (10) and (12), which results in

$$x_{\text{em}} = \frac{(1 - \alpha)x_{\text{flue}}x_{\text{cap}}}{x_{\text{cap}} - \alpha x_{\text{flue}}} \quad (13)$$

In the following several minimum separation energies are calculated at different initial gas compositions, CO_2 capture efficiencies, and separation temperatures.

Table 1: Min. separation work (in kJ/kgCO_2) for different initial gas & capture conditions ($n_{\text{flue}} = 1$ mol).

CO ₂ capture efficiency α	$W_{\text{sep}}^{\text{min}}$ at 298 K	$W_{\text{sep}}^{\text{min}}$ at 313 K	$W_{\text{sep}}^{\text{min}}$ at 313 K
	$x_{\text{flue}} = 0.12, x_{\text{cap}} = 1$	$x_{\text{flue}} = 0.13, x_{\text{cap}} = 1$	$x_{\text{flue}} = 0.13, x_{\text{cap}} = 0.9$
1	172.2 ⁴	175.8 ⁵	154.4
0.9	158.1 ^{4,6}	161.1 ⁵	139.8

Finally, the value corresponding to parasitic energy can be estimated. In our model of parasitic energy no constant CO_2 capture efficiency is assumed. In an ideal case, however, i.e. the material adsorb all the present CO_2 , α equals to 1. The CO_2 mole fraction in the flue gas is set to be $x_{\text{flue}} = 0.14$, $T = 313$ K, and the mole fraction at desorption conditions is 99:1, i.e. $x_{\text{cap}} = 0.99$, and $x_{\text{em}} = 0$ as pure inert gas is emitted. The resulting minimum energy for separation equals $W_{\text{sep}}^{\text{min}} = 167.7$ kJ/kgCO_2 . Analogically, the minimum energy for $\alpha = 0.9$ yields in $W_{\text{sep}}^{\text{min}} = 153.1$ kJ/kgCO_2 .

3 Envelope lines for coal and natural gas

To specify more reliable envelope lines for the coal and natural gas results, we predicted parasitic energies using the dataset published by Lin et. al.⁷ based on the IAST model for a bi-component mixture gas. The functional form applied to fit the envelope lines was determined to be

$$f(x) = \frac{a}{x^n} + b \cdot x^m \quad (14)$$

To get a reasonable dataset of values which represents the envelope of each gas composition to perform the fitting, we applied the method of bins in x- and y-direction.

Figure 2a and 2b show the parasitic energy results for the coal and natural gas composition, respectively. The red circles illustrate the parasitic energies of the IZA zeolite structures as well as the predicted structures. As dashed lines the fitted envelopes for both flue gases are shown. Furthermore, the fit functions for both envelope lines are included.

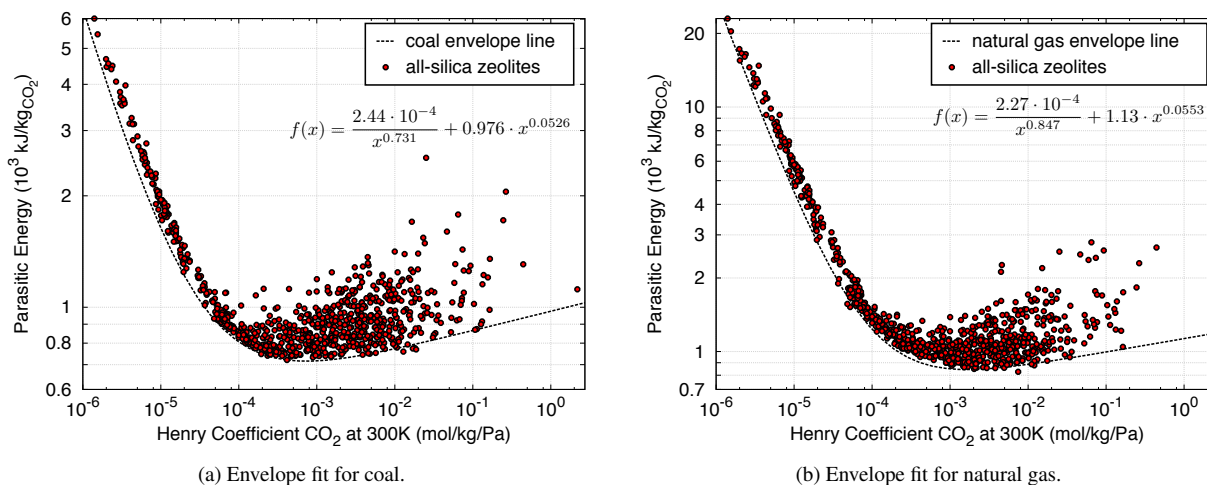


Figure 2: Parasitic energy envelope lines for coal and natural gas of IZA zeolites and predicted structures⁷. Red circles represent the parasitic energies of these all-silica zeolites. Dashed lines indicate the corresponding envelopes. The fitting parameters for the coal case are $a = 2.44 \cdot 10^{-4}$, $n = 0.731$, $b = 0.976$, and $m = 0.0526$. The natural gas fitting parameters were calculated to be $a = 2.27 \cdot 10^{-4}$, $n = 0.847$, $b = 1.13$, and $m = 0.0553$.

4 Heat capacity impact on parasitic energy

Another very important parameter for the parasitic energy calculation is the specific heat capacity C_p of each material. Unfortunately, only a limited number of specific heat capacities has already been measured and reported in literature. An alternative way to get the specific heat capacities is by determine them by quantum calculations. Density functional theory calculations are quite expensive and time-consuming, hence not a preferable option.

Regarding this study a center value ($C_p = 0.985$ J/gK), based on a lower and upper bound was used in most cases to compute the parasitic energy. The limits applied on the heat capacity are reported by Mu and Walton in⁸ and correspond to true specific heat capacities values of MOF-5 ($C_p = 0.761$ J/gK, lower bound) and LaCu-MOF ($C_p = 1.21$ J/gK, upper bound) at 333 K. Additionally, the heat capacity is assumed not to be a strong function of the process temperature and thus is kept constant in this work.

Figure 3 shows the parasitic energy results for coal including the values for the upper, lower, and center heat capacity values. All results based on the center value are depicted as circles. The colors correspond the different classes of materials, respectively. The parasitic energy uncertainty caused by using an upper and lower heat capacity limits are illustrated as error bars. Further, included is the coal envelope line (dashed line) as well as the current state-of-art technology MEA (dotted line). As shown in figure 3 the main impact of the specific heat capacity on the parasitic energy is restricted to materials indicating low henry coefficients of CO_2 ($k_H = 2 \cdot 10^{-6} - 6 \cdot 10^{-5}$ mol/kgPa). Their ability and preference to adsorb CO_2 is already low, thus the sensible heat term (equation (1) first term in main article), which contains the heat capacity value influences the final parasitic energy result more. Compared materials indicating promising parasitic energies appear to be almost independent from the heat capacity uncertainty. The error bars for the materials within CO_2 henry coefficients of $k_H = 1 \cdot 10^{-4} - 1 \cdot 10^{-1}$ mol/kgPa are smaller then the actual symbol, which means that the effect of the desorption heat requirement (equation (1) second term in main article) is dominating the final parasitic energy result and the influence of the sensible heat is nearly negligible.

Although the correct specific heat capacities are not available the results based on the center value provide a sophisticated guess in which parasitic energy region the materials are to be expected.

The strategy of choosing a heat capacity value was necessary, in particular, for hypothetical and not yet synthesized materials. For the heat capacity estimation of the zeolites with exchanged cations a different approach⁹ was applied.

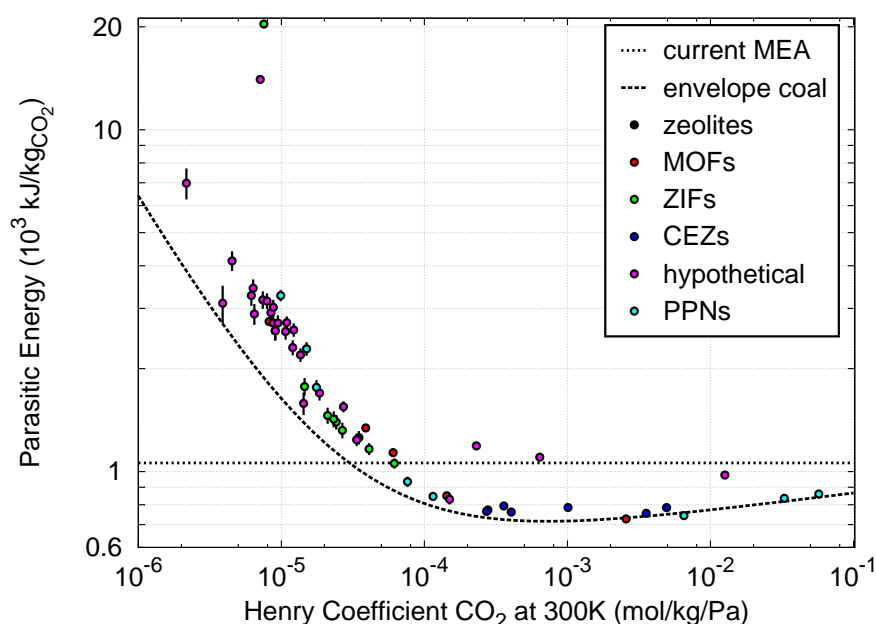


Figure 3: Impact of specific heat capacity on parasitic energy. Circle indicate parasitic energy results using center value as heat capacity. Error bars illustrate the parasitic energy uncertainty by applying the upper and lower limits. Dashed line corresponds to the coal envelope line. As a dotted line the current state-of-art technology of MEA is shown.

5 Energy loss calculation

To estimate the energy loss (EL) caused by applying CCS to power plants the parasitic energy results (PE) needs to be normalized by the total energy that is provided per amount produced CO_2 .

Based on the values reported by U.S. Energy Information Administration¹ coal and natural gas produce the following amount of total energy per unit of fuel:

$$\text{coal} = 1,842 \text{ kWh/t} \quad \text{natural gas} = 127 \text{ kWh/Mcf.}$$

Expressed in $\text{kJ/kg}_{\text{fossil fuel}}$ these values correspond to

$$\text{coal} = 6,631.2 \text{ kJ/kg} \quad \text{natural gas} = 21,023.3 \text{ kJ/kg}$$

(using the conversion factors: $1 \text{ cf} = 0.02832 \text{ m}^3$, $1 \text{ kWh} = 3.6 \cdot 10^6 \text{ J}$, and $\rho_{\text{natural gas}} = 0.768 \text{ kg/m}^3$). To normalize the predicted parasitic energies the amount of produced CO_2 per amount consumed fossil fuel needs to be known.

These can also be found on the U.S. Energy Information Administration homepage:²

$$\begin{aligned} \text{coal (Sub-bituminous)} &= 2.16 \text{ Lbs}_{\text{CO}_2}/\text{kWh} = 1.80 \text{ kg}_{\text{CO}_2}/\text{kg}_{\text{coal}} \\ \text{natural gas} &= 1.22 \text{ Lbs}_{\text{CO}_2}/\text{kWh} = 3.23 \text{ kg}_{\text{CO}_2}/\text{kg}_{\text{natural gas}} \end{aligned}$$

(conversion factor: $1 \text{ Lbs} = 0.4536 \text{ kg}$).

The energy loss in case of coal and natural gas is included in table 2 for materials under investigation.

¹U.S. Energy Information Administration, How much coal, natural gas, or petroleum is used to generate a kilowatt-hour of electricity? (eia, Jan. 2014); <http://www.eia.gov/tools/faqs/faq.cfm?id=667&t=2>

²U.S. Energy Information Administration, How much carbon dioxide (CO_2) is produced per kilowatthour when generating electricity with fossil fuels? (eia, Jan. 2014); <http://www.eia.gov/tools/faqs/faq.cfm?id=74&t=11>

6 Summarized data

Tables 2 & 3 summarize all used and calculated values for all investigated materials. The majority of parasitic energy results are shown as upper, center and lower value, due to the uncertainty of the specific heat capacity. For materials only indicating one parasitic energy value the specific heat capacity was either estimated by quantum calculations or a reported value was found in the literature. All heat of adsorptions, Henry coefficients, and saturation loadings are based on $T = 300$ K, parasitic energies are calculated by using IAST.

Table 2: Summarized parameters for all materials. Units: Material density ρ (kg/m³), specific heat capacity C_p (J/kgK), heat of adsorption ΔH (kJ/mol), Henry coefficient k_H (mol/kgPa), saturation loading q_{sat} (mol/kg). Parameters ΔH , k_H , and q_{sat} refer to $T = 300$ K.

structure	ρ	C_p	CO ₂						N ₂		
			ΔH_1	$k_{H,1}$	$q_{sat,1}$	ΔH_2	$k_{H,2}$	$q_{sat,2}$	ΔH_1	$k_{H,1}$	$q_{sat,1}$
CaA	1514.0	985 ¹²¹⁰ ₇₆₁	-58.66	4.93e-03	3.94	-14.53	3.54e-05	1.6	-13.02	6.17e-06	5.54
CaX	1426.0	985 ¹²¹⁰ ₇₆₁	-41.02	1.01e-03	3.19	-30.65	5.09e-05	3.55	-5.06	4.08e-06	6.74
MgA	1514.0	985 ¹²¹⁰ ₇₆₁	-36.72	3.59e-04	3.58	-26.5	8.89e-06	1.57	-24.73	2.89e-06	5.15
MgX	1426.0	985 ¹²¹⁰ ₇₆₁	-40.85	4.05e-04	3.38	-32.58	3.82e-05	3.3	-24.93	2.05e-06	6.69
NaA	1514.0	985 ¹²¹⁰ ₇₆₁	-30.12	2.72e-04	2.4	-30.09	1.71e-05	1.57	-8.34	8.86e-07	3.97
NaX	1426.0	985 ¹²¹⁰ ₇₆₁	-50.11	3.55e-03	2.5	-37.4	1.77e-04	3.81	-15.11	3.55e-06	6.31
PS-MFI	1838.0	863 ¹²¹⁰ ₇₆₁	-26.23	3.48e-05	3.44				-22.26	1.77e-06	3.439
Mg-MOF-74	914.88	896	-37.36	2.57e-03	6.32	-19.81	2.77e-05	9.08	-18.73	1.1e-05	5.0
Zn-MOF-74	1219.39	684	-25.02	1.43e-04	10.21				-13.45	3.01e-06	10.18
Co-MOF-74	1180.54	985 ¹²¹⁰ ₇₆₁	-36.54	3.0e-04	8.66				-12.4	6.64e-06	8.66
Ni-MOF-74	1194.09	985 ¹²¹⁰ ₇₆₁	-45.87	4.71e-04	2.41	-20.69	7.92e-05	6.59	-25.32	1.25e-05	6.65
MOF-177	426.74	840	-13.71	8.21e-06	25.0				-10.89	1.83e-06	5.0
CuBTC	948.8	1158	-27.49	6.05e-05	17.58				-15.35	2.62e-06	5.63
CuBTTri	789.0	985 ¹²¹⁰ ₇₆₁	-24.26	3.89e-05	42.6				-1.92	2.37e-06	5.0
mmen-CuBTTri	1059.0	985 ¹²¹⁰ ₇₆₁	-53.0	2.78e-04	4.68				-24.55	1.24e-06	0.3
UMCM-1	429.0	851.3	-10.92	9.87e-06	150.0				-5.45	1.75e-06	55.0
SIFSIX-3-Cu	1728.0	985	-47.52	3.14e-02	2.4	-3.76	2.09e-06	0.4	-10.81	1.93e-06	2.8
SIFSIX-3-Zn	1574.0	985	-41.5	3.47e-03	2.6	-27.87	1.32e-06	0.286	-12.21	2.91e-06	2.886
ZIF-8	949.0	985 ¹²¹⁰ ₇₆₁	-20.96	7.55e-06	14.2				-13.2	2.33e-05	122.2
ZIF-68	900.77	985 ¹²¹⁰ ₇₆₁	-23.99	2.11e-05	5.836				-15.44	1.18e-06	4.291
ZIF-69	998.74	985 ¹²¹⁰ ₇₆₁	-22.21	2.42e-05	6.237				-13.2	1.37e-06	5.948
ZIF-70	747.24	985 ¹²¹⁰ ₇₆₁	-19.88	1.45e-05	8.477				-14.28	1.30e-06	1.728
ZIF-78	1023.9	985 ¹²¹⁰ ₇₆₁	-26.63	6.17e-05	3.569				-13.3	1.80e-06	3.367
ZIF-79	937.03	985 ¹²¹⁰ ₇₆₁	-25.98	2.33e-05	3.564				-14.85	1.18e-06	1.883
ZIF-81	1124.27	985 ¹²¹⁰ ₇₆₁	-25.52	2.67e-05	3.878				-14.23	1.19e-06	2.173
ZIF-82	815.86	985 ¹²¹⁰ ₇₆₁	-24.92	4.10e-05	4.944				-13.79	1.52e-06	3.414
PPN-4	284.1	985 ¹²¹⁰ ₇₆₁	-13.86	9.9e-06	120.0				-6.61	3.02e-06	8.2
PPN-6	325.0	985 ¹²¹⁰ ₇₆₁	-16.35	1.5e-05	12.0				-7.31	2.9e-06	0.5
PPN-6-CH ₂ Cl	528.0	985 ¹²¹⁰ ₇₆₁	-20.05	1.76e-05	10.4				-8.56	1.76e-06	0.63
PPN-6-SO ₃ H	642.0	985 ¹²¹⁰ ₇₆₁	-27.82	7.62e-05	6.0				-9.27	2.32e-06	0.4
PPN-6-SO ₃ Li	666.0	985 ¹²¹⁰ ₇₆₁	-30.27	1.15e-04	5.0				-7.13	2.6e-06	0.4
PPN-6-CH ₂ DETA	805.0	985 ¹²¹⁰ ₇₆₁	-45.33	5.71e-02	5.35				-17.99	7.65e-07	0.1
PPN-6-CH ₂ TAEA	982.5	985 ¹²¹⁰ ₇₆₁	-35.01	3.28e-02	4.82				-14.91	9.38e-07	0.02
PPN-6-CH ₂ TETA	883.8	985 ¹²¹⁰ ₇₆₁	-48.23	6.52e-03	4.77				-18.29	6.99e-07	0.04
ZIF-36-CAG	2006.5	985 ¹²¹⁰ ₇₆₁	-51.77	1.26e-02	1.48				-25.38	6.48e-06	1.48
ZIF-36-FRL	1808.87	985 ¹²¹⁰ ₇₆₁	-40.66	1.50e-04	2.01	-24.39	2.15e-06	1.01	-18.75	4.74e-07	3.02
ZIF-39-DIA	1009.17	985 ¹²¹⁰ ₇₆₁	-28.88	1.43e-05	10.35				-16.34	5.4e-07	10.35
ZIF-39-ZNI	1497.35	985 ¹²¹⁰ ₇₆₁	-30.47	2.17e-06	1.29				-22.36	9.74e-07	1.29
ZIF-40-GIS	1254.51	985 ¹²¹⁰ ₇₆₁	-33.26	2.31e-04	2.21	-3.66	5.38e-06	3.76	-22.14	1.03e-05	5.97
ZIF-116-CAG	1353.83	985 ¹²¹⁰ ₇₆₁	-37.81	6.41e-04	2.14	-20.79	2.06e-06	2.51	-24.35	1.53e-05	4.65
ZIF-116-MER	850.95	985 ¹²¹⁰ ₇₆₁	-22.04	2.72e-05	16.57				-11.51	2.38e-06	16.57
ZIF-116-SOD	855.31	985 ¹²¹⁰ ₇₆₁	-17.95	1.2e-05	14.15				-11.27	2.01e-06	14.15
HMOF-MOF-5	572.98	985 ¹²¹⁰ ₇₆₁	-14.96	8.45e-06	27.37				-8.01	1.97e-06	27.37
HMOF-16	701.06	985 ¹²¹⁰ ₇₆₁	-22.68	3.36e-05	30.47				-8.37	1.61e-06	1.54
HMOF-27	777.34	985 ¹²¹⁰ ₇₆₁	-12.53	4.52e-06	52.91				-8.42	1.7e-06	1.48
HMOF-96	576.92	985 ¹²¹⁰ ₇₆₁	-14.49	7.12e-06	138.61				-8.59	2.26e-05	1.71
HMOF-163	1000.38	985 ¹²¹⁰ ₇₆₁	-17.63	8.77e-06	15.07				-11.68	1.93e-06	1.02

HMOF-469	873.26	985 ¹²¹⁰ ₇₆₁	-15.56	6.47e-06	34.32	-8.37	1.25e-06	14.79
HMOF-541	905.88	985 ¹²¹⁰ ₇₆₁	-17.99	9.05e-06	20.5	-10.91	1.75e-06	0.96
HMOF-602	905.88	985 ¹²¹⁰ ₇₆₁	-17.99	9.07e-06	19.75	-10.91	1.75e-06	1.03
HMOF-611	648.95	985 ¹²¹⁰ ₇₆₁	-17.11	9.46e-06	51.07	-9.36	2.05e-06	1.68
HMOF-646	245.77	985 ¹²¹⁰ ₇₆₁	-12.59	7.95e-06	81.57	-5.49	2.64e-06	81.57
HMOF-785	639.42	985 ¹²¹⁰ ₇₆₁	-15.24	8.78e-06	43.51	-9.47	2.42e-06	1.66
HMOF-972	670.41	985 ¹²¹⁰ ₇₆₁	-14.75	6.35e-06	58.92	-9.29	1.91e-06	1.58
HMOF-992	624.98	985 ¹²¹⁰ ₇₆₁	-21.31	1.85e-05	24.41	-8.35	1.55e-06	24.41
HMOF-1041	409.13	985 ¹²¹⁰ ₇₆₁	-14.65	1.09e-05	41.81	-7.45	2.44e-06	41.81
HMOF-1055	711.3	985 ¹²¹⁰ ₇₆₁	-16.03	1.22e-05	27.59	-10.51	2.94e-06	1.58
HMOF-1631	834.9	985 ¹²¹⁰ ₇₆₁	-17.15	1.07e-05	27.62	-10.91	2.35e-06	1.12
HMOF-1708	765.19	985 ¹²¹⁰ ₇₆₁	-15.39	7.42e-06	32.57	-10.0	2.1e-06	1.37
HMOF-1927	849.84	985 ¹²¹⁰ ₇₆₁	-14.77	6.17e-06	32.86	-9.57	1.67e-06	1.09
HMOF-1996	612.16	985 ¹²¹⁰ ₇₆₁	-14.67	7.94e-06	61.59	-8.94	2.26e-06	1.71
HMOF-2368	226.63	985 ¹²¹⁰ ₇₆₁	-12.17	7.65e-06	100.01	-5.27	2.78e-06	100.01

The parameters presented in tab. 2 are based on the following experimental references: MOFs^{3,10–21}, PPNs^{22,23}, ZIFs^{24–26}, CEZs². Properties of hypothetical materials were predicted by GCMC simulations.

Table 3: Summarized results for all gas compositions & regeneration strategies. Units: Parasitic energies PE_{comp} (MJ/kgCO₂), and energy loss EL_{comp} (%). Heating energy and compression work for PSA & TSA are also shown in (MJ/kgCO₂), respectively. All shown PE results are based on IAST.

structure	PE _{coal}	EL _{coal}	PE _{NG}	EL _{NG}	PE _{air}	PSA		TSA	
						heating	compression	heating	compression
CaA	0.784 ^{0.794} _{0.774}	21.3	0.943	14.5	3.6	0.208	0.576	0.557	0.37
CaX	0.785 ^{0.796} _{0.774}	21.3	1.06	16.3	17.6	0.167	0.618	0.595	0.395
MgA	0.793 ^{0.807} _{0.778}	21.5	1.17	18	62	0.178	0.615	0.77	0.408
MgX	0.76 ^{0.774} _{0.749}	20.6	1.06	16.3	36.8	0.186	0.574	0.625	0.39
NaA	0.765 ^{0.783} _{0.745}	20.8	1.05	16.1	85.6	0.177	0.588	1.19	0.382
NaX	0.754 ^{0.767} _{0.744}	20.5	0.925	14.2	4.57	0.191	0.563	0.528	0.371
PS-MFI	1.23 ^{1.31} _{1.2}	33.3	2.9	44.6	1.11e+03	0.322	0.904	4.62	0.615
Mg-MOF-74	0.727	19.7	0.959	14.7	16	0.142	0.585	0.463	0.378
Zn-MOF-74	0.85	23.1	1.56	23.9	250	0.134	0.716	1.11	0.47
Co-MOF-74	0.907 ^{0.918} _{0.896}	24.6	1.71	26.3	91.7	0.168	0.739	0.659	0.494
Ni-MOF-74	0.96 ^{0.97} _{0.95}	26.1	1.74	26.8	110	0.182	0.778	0.943	0.5
MOF-177	2.75	74.6	9.79	150	6.04e+04	0.659	2.09	82.8	2
CuBTC	1.14	30.8	2.65	40.7	723	0.265	0.872	3.07	0.599
CuBTTri	1.34 ^{1.39} _{1.3}	36.4	3.58	55	1.33e+03	0.27	1.07	4.81	0.781
mmen-CuBTTri	0.752 ^{0.788} _{0.757}	20.4	1.11	17	30	0.248	0.505	0.574	0.363
UMCM-1	2.38	64.7	8.24	127	2.81e+05	0.515	1.87	111	1.84
SIFSIX-3-Cu	0.94	25.5	0.963	14.8	1.62	0.211	0.729	1.4	0.357
SIFSIX-3-Zn	0.805	21.8	0.907	13.9	5.81	0.201	0.604	0.881	0.364
ZIF-8	20.4 ^{20.6} _{20.2}	553	89.8	1.38e+03	2.89e+04	1.89	18.5	46.9	16.4
ZIF-68	1.46 ^{1.54} _{1.38}	39.6	3.85	59.2	2.64e+03	0.438	1.02	9.64	0.714
ZIF-69	1.4 ^{1.46} _{1.33}	37.9	3.63	55.8	2.76e+03	0.381	1.01	9.35	0.719
ZIF-70	1.77 ^{1.88} _{1.67}	48.1	5.28	81.1	7.89e+03	0.557	1.22	20.7	0.925
ZIF-78	1.06 ^{1.09} _{1.02}	28.7	2.22	34.1	653	0.25	0.807	3.22	0.538
ZIF-79	1.42 ^{1.5} _{1.34}	38.7	3.68	56.5	1.96e+03	0.433	0.992	8.09	0.708
ZIF-81	1.32 ^{1.39} _{1.25}	35.8	3.26	50.1	1.69e+03	0.4	0.92	7.06	0.624
ZIF-82	1.16 ^{1.21} _{1.12}	31.6	2.68	41.2	1.18e+03	0.289	0.875	4.85	0.594
PPN-4	3.27 ^{3.4} _{3.15}	88.8	12.3	188	6.43e+04	0.627	2.64	85.1	2.67

6 SUMMARIZED DATA

PPN-6	2.29 ^{2.39} _{2.18}	62	8.2	126	3e+04	0.53	1.76	46.7	1.55
PPN-6-CH ₂ Cl	1.76 ^{1.85} _{1.67}	47.9	5.48	84.2	7.98e+03	0.491	1.27	19.6	0.976
PPN-6-SO ₃ H	0.934 ^{0.966} _{0.901}	25.4	2.07	31.8	638	0.23	0.704	2.64	0.454
PPN-6-SO ₃ Li	0.846 ^{0.871} _{0.82}	23	1.7	26.2	338	0.202	0.644	1.69	0.419
PPN-6-CH ₂ DETA	0.86 ^{0.876} _{0.843}	23.3	0.88	13.5	1.21	0.21	0.65	0.815	0.356
PPN-6-CH ₂ TAEA	0.835 ^{0.85} _{0.816}	22.7	0.858	13.2	1.65	0.187	0.648	1.2	0.356
PPN-6-CH ₂ TETA	0.742 ^{0.756} _{0.731}	20.2	0.807	12.4	1.95	0.209	0.534	0.511	0.358
ZIF-36-CAG	0.977 ^{0.997} _{0.949}	26.5	1.02	15.7	3.24	0.242	0.735	1.48	0.361
ZIF-36-FRL	0.829 ^{0.858} _{0.8}	22.5	1.21	18.6	72.6	0.253	0.576	1.18	0.384
ZIF-39-DIA	1.58 ^{1.7} _{1.46}	43	4.2	64.6	2.26e+03	0.623	0.96	10.5	0.661
ZIF-39-ZNI	6.98 ^{7.7} _{6.23}	189	26.3	404	4.58e+04	3.57	3.41	143	4.22
ZIF-40-GIS	1.19 ^{1.21} _{1.17}	32.3	2.5	38.4	418	0.208	0.981	2.57	0.706
ZIF-116-CAG	1.1 ^{1.12} _{1.09}	29.9	1.93	29.6	124	0.199	0.903	1.17	0.542
ZIF-116-MER	1.55 ^{1.61} _{1.49}	42	4.38	67.3	2.59e+03	0.346	1.2	8.17	0.901
ZIF-116-SOD	2.3 ^{2.42} _{2.19}	62.6	7.63	117	1.25e+04	0.604	1.7	29.2	1.38
HMOF-MOF-5	2.92 ^{3.07} _{2.77}	79.2	10.4	160	4.18e+04	0.753	2.16	69.2	2.04
HMOF-16	1.24 ^{1.29} _{1.19}	33.6	3.14	48.3	1.98e+03	0.303	0.936	6.55	0.65
HMOF-27	4.13 ^{4.41} _{3.85}	112	15.9	244	2.11e+05	1.33	2.8	226	2.9
HMOF-96	14 ^{14.3} _{13.8}	381	63.6	978	1.69e+05	1.43	12.6	184	13.1
HMOF-163	2.72 ^{2.89} _{2.56}	73.9	9.58	147	2.26e+04	0.834	1.89	47.1	1.64
HMOF-469	2.89 ^{3.09} _{2.69}	78.4	10.1	155	4.4e+04	0.966	1.92	79.5	1.7
HMOF-541	2.58 ^{2.74} _{2.42}	70.1	8.95	138	2.08e+04	0.802	1.78	44.1	1.49
HMOF-602	2.58 ^{2.74} _{2.42}	70.1	8.94	137	2.05e+04	0.798	1.78	43.7	1.49
HMOF-611	2.72 ^{2.87} _{2.57}	73.8	9.6	148	2.47e+04	0.738	1.98	47.9	1.77
HMOF-646	3.62 ^{3.77} _{3.48}	98.3	13.8	212	2.09e+05	0.711	2.91	146	3.12
HMOF-785	3.02 ^{3.18} _{2.87}	82.1	11.1	170	4.13e+04	0.779	2.25	67.8	2.06
HMOF-972	3.44 ^{3.65} _{3.23}	93.4	12.8	197	7.05e+04	1.01	2.43	106	2.33
HMOF-992	1.7 ^{1.78} _{1.61}	46.1	4.98	76.5	4.57e+03	0.443	1.25	13.5	0.946
HMOF-1041	2.73 ^{2.84} _{2.61}	74	9.68	149	3.62e+04	0.592	2.14	57.3	2
HMOF-1055	2.6 ^{2.71} _{2.48}	70.5	9.22	142	2.24e+04	0.61	1.99	41.1	1.74
HMOF-1631	2.57 ^{2.71} _{2.43}	69.8	9.03	139	2.05e+04	0.695	1.87	41	1.56
HMOF-1708	3.18 ^{3.37} ₃	86.4	11.7	180	4.74e+04	0.913	2.27	78.7	2.12
HMOF-1927	3.27 ^{3.49} _{3.05}	88.9	12	185	6.73e+04	1.06	2.22	105	2.05
HMOF-1996	3.15 ^{3.32} _{2.99}	85.6	11.6	179	5.45e+04	0.833	2.32	83.5	2.23
HMOF-2368	3.82 ^{3.97} _{3.68}	104	14.8	227	7.6e+05	0.722	3.1	171	3.37

References

- [1] A. L. Dzubak, L.-C. Lin, J. Kim, J. A. Swisher, R. Poloni, S. N. Maximoff, B. Smit and L. Gagliardi, *Nature Chemistry*, 2012, **4**, 810–816.
- [2] T.-H. Bae, M. R. Hudson, J. A. Mason, W. L. Queen, J. J. Dutton, K. Sumida, K. J. Micklash, S. S. Kaye, C. M. Brown and J. R. Long, *Energy & Environmental Science*, 2013, **6**, 128.
- [3] T. M. McDonald, D. M. D'Alessandro, R. Krishna and J. R. Long, *Chemical Science*, 2011, **2**, 2022.
- [4] *Direct Air Capture of CO₂ with Chemicals*, 2011, <http://www.aps.org/policy/reports/assessments/upload/dac2011.pdf>.
- [5] A. S. Bhowan and B. C. Freeman, *Environmental science & technology*, 2011, **45**, 8624–32.
- [6] B. Smit, J. R. Reimer, C. M. Oldenburg and I. C. I. C. Bourg, *Introduction to Carbon Capture and Sequestration*, Imperial College Press, London, 1st edn., 2014.
- [7] L.-C. Lin, A. H. Berger, R. L. Martin, J. Kim, J. A. Swisher, K. Jariwala, C. H. Rycroft, A. S. Bhowan, M. W. Deem, M. Haranczyk and B. Smit, *Nature materials*, 2012, **11**, 633–41.
- [8] B. Mu and K. S. Walton, *The Journal of Physical Chemistry C*, 2011, **115**, 22748–22754.
- [9] P. Vieillard, *European Journal of Mineralogy*, 2010, **22**, 823–836.
- [10] P. Aprea, D. Caputo, N. Gargiulo, F. Iucolano and F. Pepe, *Journal of Chemical & Engineering Data*, 2010, **55**, 3655–3661.
- [11] P. Chowdhury, S. Mekala, F. Dreisbach and S. Gumma, *Microporous and Mesoporous Materials*, 2012, **152**, 246–252.
- [12] P. D. C. Dietzel, V. Besikiotis and R. Blom, *Journal of Materials Chemistry*, 2009, **19**, 7362.
- [13] P. D. C. Dietzel, R. Blom and H. Fjellvåg, *European Journal of Inorganic Chemistry*, 2008, **2008**, 3624–3632.
- [14] L. Grajciar, A. D. Wiersum, P. L. Llewellyn, J.-S. Chang and P. Nachtigall, *The Journal of Physical Chemistry C*, 2011, **115**, 17925–17933.
- [15] Z. Liang, M. Marshall and A. L. Chaffee, *Energy & Fuels*, 2009, **23**, 2785–2789.
- [16] J. A. Mason, K. Sumida, Z. R. Herm, R. Krishna and J. R. Long, *Energy & Environmental Science*, 2011, **4**, 3030.
- [17] B. Mu, P. M. Schoenecker and K. S. Walton, *The Journal of Physical Chemistry C*, 2010, **114**, 6464–6471.
- [18] J. M. Simmons, H. Wu, W. Zhou and T. Yildirim, *Energy & Environmental Science*, 2011, **4**, 2177.
- [19] K. Uemura, A. Maeda, T. K. Maji, P. Kanoo and H. Kita, *European Journal of Inorganic Chemistry*, 2009, **2009**, 2329–2337.
- [20] P. Nugent, Y. Belmabkhout, S. D. Burd, A. J. Cairns, R. Luebke, K. Forrest, T. Pham, S. Ma, B. Space, L. Wojtas, M. Eddaoudi and M. J. Zaworotko, *Nature*, 2013, **495**, 80–4.
- [21] O. Shekhah, Y. Belmabkhout, Z. Chen, V. Guillerm, A. Cairns, K. Adil and M. Eddaoudi, *Nature communications*, 2014, **5**, 4228.
- [22] W. Lu, J. P. Sculley, D. Yuan, R. Krishna, Z. Wei and H.-C. Zhou, *Angewandte Chemie (International ed. in English)*, 2012, **51**, 7480–4.
- [23] W. Lu, D. Yuan, J. Sculley, D. Zhao, R. Krishna and H.-C. Zhou, *Journal of the American Chemical Society*, 2011, **133**, 18126–9.
- [24] H. Amrouche, S. Aguado, J. Pérez-Pellitero, C. Chizallet, F. Siperstein, D. Farrusseng, N. Bats and C. Nieto-Draghi, *The Journal of Physical Chemistry C*, 2011, **115**, 16425–16432.

REFERENCES

REFERENCES

- [25] R. Banerjee, H. Furukawa, D. Britt, C. Knobler, M. O’Keeffe and O. M. Yaghi, *Journal of the American Chemical Society*, 2009, **131**, 3875–7.
- [26] H. Huang, W. Zhang, D. Liu, B. Liu, G. Chen and C. Zhong, *Chemical Engineering Science*, 2011, **66**, 6297–6305.